

Observations of the Eyewall Structure of Typhoon Sinlaku (2008) during the Transformation Stage of Extratropical Transition

ANNETTE M. FOERSTER*

Institute for Meteorology and Climate Research, Karlsruhe Institute of Technology, Karlsruhe, Germany

MICHAEL M. BELL

Department of Meteorology, University of Hawai'i at Mānoa, Honolulu, Hawaii

PATRICK A. HARR

Department of Meteorology, Naval Postgraduate School, Monterey, California

SARAH C. JONES⁺

Institute for Meteorology and Climate Research, Karlsruhe Institute of Technology, Karlsruhe, Germany

(Manuscript received 2 October 2013, in final form 1 May 2014)

ABSTRACT

A unique dataset observing the life cycle of Typhoon Sinlaku was collected during The Observing System Research and Predictability Experiment (THORPEX) Pacific Asian Regional Campaign (T-PARC) in 2008. In this study observations of the transformation stage of the extratropical transition of Sinlaku are analyzed. Research flights with the Naval Research Laboratory P-3 and the U.S. Air Force WC-130 aircraft were conducted in the core region of Sinlaku. Data from the Electra Doppler Radar (ELDORA), dropsondes, aircraft flight level, and satellite atmospheric motion vectors were analyzed with the recently developed Spline Analysis at Mesoscale Utilizing Radar and Aircraft Instrumentation (SAMURAI) software with a 1-km horizontal- and 0.5-km vertical-node spacing. The SAMURAI analysis shows marked asymmetries in the structure of the core region in the radar reflectivity and three-dimensional wind field. The highest radar reflectivities were found in the left of shear semicircle, and maximum ascent was found in the downshear left quadrant. Initial radar echos were found slightly upstream of the downshear direction and downdrafts were primarily located in the upshear semicircle, suggesting that individual cells in Sinlaku's eyewall formed in the downshear region, matured as they traveled downstream, and decayed in the upshear region. The observed structure is consistent with previous studies of tropical cyclones in vertical wind shear, suggesting that the eyewall convection is primarily shaped by increased vertical wind shear during step 2 of the transformation stage, as was hypothesized by Klein et al. A transition from active convection upwind to stratiform precipitation downwind is similar to that found in the principal rainband of more intense tropical cyclones.

1. Introduction

During extratropical transition (ET), the structure of tropical cyclones (TCs) changes significantly. Decreased

* Current affiliation: Department of Meteorology, University of Hawai'i at Mānoa, Honolulu, Hawaii.

⁺ Current affiliation: Deutscher Wetterdienst, Offenbach, Germany.

Corresponding author address: Annette M. Foerster, Department of Meteorology, University of Hawai'i at Mānoa, 2525 Correa Rd., Honolulu, HI 96822.
E-mail: foerster@hawaii.edu

sea surface temperatures (SSTs), increased vertical wind shear (VWS), and the interaction with the baroclinic zone result in changes of both intensity and structure. Based on a climatology of 30 tropical cyclones in the western North Pacific, Klein et al. (2000) split the extratropical transition into two distinct stages: the transformation stage and the reintensification stage. The transformation stage starts when the storm first adopts an asymmetric appearance, and ends when the storm reaches its maximum central pressure and exhibits characteristics of a baroclinic cyclone, with the center being embedded in cold, descending air. Klein et al.

(2000) subdivided the transformation stage and created a conceptual three-step model of the transformation stage of ET in the western North Pacific. A detailed modeling study by [Ritchie and Elsberry \(2001\)](#) further elucidated the physical processes occurring during these three steps. The first step consists of the interaction with decreased SSTs and the influence of colder, drier, environmental air. The second step consists of the interaction with increased VWS as the TC approaches the baroclinic zone, and the third step consists of the interaction with the baroclinic zone itself, which leads to frontogenesis and shapes the baroclinic characteristics of the transitioning storm.

[Klein et al. \(2000\)](#) used satellite imagery and the Navy Operational Global Atmospheric Prediction System (NOGAPS) analyses with a resolution of $1^\circ \times 1^\circ$ for their study, and [Ritchie and Elsberry \(2001\)](#) used U.S. Navy Coupled Ocean–Atmosphere Model Prediction System (COAMPS) mesoscale model analyses with a horizontal resolution of 15 km. Thus, even though they were able to describe the larger-scale changes in the structure of a transitioning storm, a detailed analysis of the inner-core processes, and specifically of the processes in the eyewall, was beyond the scope of their studies.

High-resolution observations in the core region of TCs during extratropical transition are still rare, and to the authors' knowledge, there is no previous observational study investigating the detailed inner core structure of a TC during the transformation stage of extratropical transition. As part of The Observing System Research and Predictability Experiment (THORPEX) Pacific Asian Regional Campaign (T-PARC) and Tropical Cyclone Structure 2008 (TCS08) field campaign, the Naval Research Laboratory (NRL) P-3 and the U.S. Air Force (USAF) WC-130 conducted flights into the inner core region of Typhoon Sinlaku, with the P-3 carrying the Electra Doppler Radar (ELDORA). A unique dataset including a complete view of Sinlaku's eyewall convection by radar and the release of several dropsondes in the inner core region enables an unprecedented, detailed view of the eyewall structure of a TC during the transformation stage. As will be shown later, the primary environmental factor impacting Sinlaku at the time of observation was VWS, which suggests that the storm was sampled during step 2 of the transformation stage. A companion paper by [Quinting et al. \(2014\)](#) documents the structural changes on the following day as interaction with the baroclinic zone occurred, defined by [Klein et al. \(2000\)](#) as step 3 of the transformation stage.

The effects of VWS on the structure of TCs have been studied in detail for mature hurricanes, and it has long

been recognized that VWS is an important environmental influence on the intensity and structure of the TC. Generally, VWS is viewed as a negative factor in TC development that impedes intensification or weakens the storm, but the interaction can be complex. Statistics across many storms indicate a negative correlation between VWS and intensity change ([Kaplan and DeMaria 2003](#); [DeMaria et al. 2005](#)); however, there are also examples where TCs undergo intensification in high or increasing VWS ([Reasor et al. 2009](#); [Nguyen and Molinari 2012](#)). To improve the ability to forecast intensity and structure change, it is necessary to identify the physical processes by which the VWS impacts the kinematic and thermodynamic structure of the TC.

The fundamental mechanisms by which VWS affects TC structure have been investigated in several theoretical and modeling studies, both moist and dry ([Jones 1995](#); [Wang and Holland 1996](#); [Frank and Ritchie 2001](#); [Reasor et al. 2004](#); [Braun et al. 2006](#); [Riemer et al. 2010, 2013](#)). These studies show that VWS tilts the vortex and induces asymmetries in both the inner core (<100 -km radius) and outer core regions of the tropical cyclone. In the inner core region, the asymmetries are evident as azimuthal wavenumber-1 patterns in both kinematic and thermodynamic fields, including vertical velocity, potential temperature, and precipitation. [Jones \(2000\)](#) showed that VWS also impacts the low-level static stability. In her baroclinic idealized numerical simulations with TC-like vortices, the low-level stability at the radius of maximum winds (RMW) was reduced on the downtilt side of the vortex and increased on the uptilt side of the vortex.

Theory, modeling, and observations support the hypothesis that VWS can enhance the eyewall convection in the downshear left direction and suppress it on the opposite side of the storm through balanced dynamics, resulting in an asymmetric, tilted TC structure. The largest upward motions are generally located downshear and the highest radar reflectivities left of shear, as growing hydrometeors are advected cyclonically around the center. Composite studies of lightning data ([Corbosiero and Molinari 2002, 2003](#)), satellite-derived precipitation data ([Hence and Houze 2011](#)), and airborne radar data ([Reasor et al. 2013](#); [DeHart et al. 2014](#)) have confirmed a robust relationship between VWS direction and asymmetric TC convective structure. The resulting impacts on the storm intensity depend on whether the vortex and asymmetric convection can resist the shear and realign, or succumb to shear and weaken.

The sensitivity of the TC to VWS depends on both the magnitude and depth of the shear, and the characteristics of the vortex. As a TC approaches the midlatitudes, the magnitude of VWS generally increases and TCs

undergoing extratropical transition are exposed to significant amounts of VWS. Davis et al. (2008) simulated six Atlantic hurricanes during extratropical transition and found that TCs can either resist the shear through precession, form an entirely new center, or develop into a baroclinic cyclone. Statistics suggest that increased horizontal vortex scale, increased vortex strength, and increased Coriolis parameter all increase the resistance of the TC to VWS (DeMaria 1996). Vortex resilience to VWS is likely due to dynamic (Schechter et al. 2002; Reasor et al. 2004) and thermodynamic (Tang and Emanuel 2010; Riemer and Montgomery 2011) mechanisms that allow the TC to maintain vertical alignment of the circulation and prevent environmental dry air from disrupting the convection.

Our understanding on VWS impacts is based primarily on theory, modeling, and statistical composites, with only a limited number of mesoscale research observations in mature hurricanes impacted by significant VWS. Black et al. (2002) and Reasor and Eastin (2012) present observational case studies that describe the inner core structure of sheared TCs in great detail using radar and flight level data. The hurricanes investigated in these studies (Jimena, Olivia, and Guillermo) were mature hurricanes occurring in the tropical eastern Pacific. During the respective observation periods, Jimena, Olivia, and Guillermo all exhibited surface wind speeds in excess of 100 kt ($1 \text{ kt} = 0.5144 \text{ m s}^{-1}$), central pressures lower than 950 hPa, and were all located well south of 20°N .

The observations of the inner core region of Sinlaku during the transformation stage of extratropical transition presented in this paper reveal many features similar to those found in mature TCs under the influence of significant VWS, although Sinlaku was much weaker and located much farther north, just south of Japan at approximately 33°N . This corroborates the conceptual model of Klein et al. (2000), which suggests that VWS is the primary factor influencing the TC structure during the second step of the transformation stage. In addition, the eyewall convection of Sinlaku showed characteristics similar to rainbands, which may be due to the decreased overall intensity of Sinlaku compared to the previously studied TCs.

In the following sections, a detailed description of the three-dimensional structure of Sinlaku during the transformation stage of extratropical transition is presented and is compared with the structure of mature sheared storms located much farther equatorward. The dataset and analysis methodology using a recently developed tool called Spline Analysis at Mesoscale Utilizing Radar and Aircraft Instrumentation (SAMURAI) are described in section 2, with additional details in the appendix. A detailed description of the precipitation,

kinematic, and thermodynamic structure of Sinlaku's eyewall in relation to the VWS vector is presented in section 3. A discussion of the results and comparison with previous studies is presented in section 4, followed by a summary and conclusions in section 5.

2. Dataset and methodology

a. Typhoon Sinlaku

Typhoon Sinlaku was one of four typhoons investigated during the T-PARC/TCS08 field campaigns in 2008. Sinlaku was first classified as a tropical depression on 8 September (Fig. 1), forming to the east of the Philippines and then moving northwestward. After a period of rapid intensification Sinlaku reached typhoon strength at 1200 UTC 9 September. It intensified further, peaking on 10 September with a central pressure of 929 hPa and maximum winds of 125 kt. The landfall in Taiwan on 14 September considerably weakened Sinlaku. Further weakening occurred as Sinlaku recurved on 15 September and subsequently moved toward the midlatitudes. Sinlaku started its extratropical transition, but instead of completing the transformation, Sinlaku reintensified starting on 17 September (Sanabia 2010). The storm continued to intensify on 18 September (Kuo et al. 2012), and at 0000 UTC 19 September the tropical storm was again classified as a typhoon. A few hours later, Sinlaku reached a secondary peak intensity of 70 kt before it continued its extratropical transition and began its final weakening.

In the early hours of 19 September 2008 (denoted by the star in Fig. 1), just after Sinlaku was reclassified as a typhoon and was located just south of Japan, a coordinated aircraft mission was conducted into the inner core region. The flight tracks are displayed in Fig. 2. The USAF C-130 flew at 9-km altitude, and the NRL P-3 flew at 3-km altitude. Both aircraft recorded flight level in situ data and released GPS dropsondes (Hock and Franklin 1999). In addition, the NRL P-3 was equipped with the airborne Doppler radar ELDORA (Hildebrand et al. 1996). The P-3 approached Sinlaku from the south-southeast, entered the eye through a gap in the eyewall, completed a counterclockwise circle inside the eye and exited the eye to the west. This flight pattern enabled complete sampling of the eyewall in all directions. Additionally, the high sensitivity of ELDORA was able to sample cloudy regions in the eye and around the inner edge of the eyewall that are often unresolved by weather radars. The radar observations used for the analysis were made during a period of 25 min, from 0350 to 0415 UTC.

Klein et al. (2000) investigated the transformation stage of extratropical transition and found characteristic

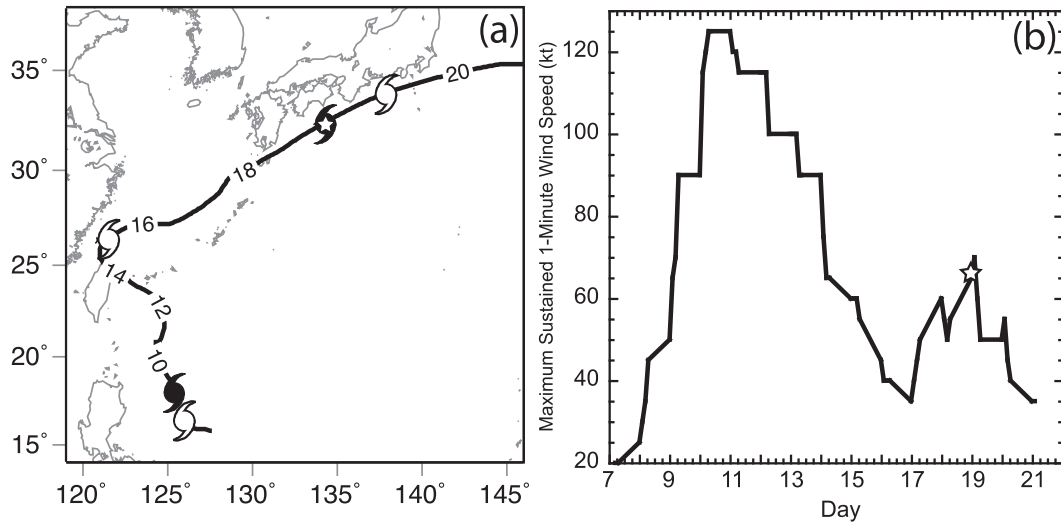


FIG. 1. Best track and intensity of Typhoon Sinlaku (2008). (a) JTWC best track from 7–21 Sep, with even days highlighted along the track. Filled symbols indicate typhoon status, and open symbols indicate tropical storm status. The star inside the filled symbol denotes the analysis time of the current study. (b) Best track wind intensity (kt), with the star denoting the analysis time.

patterns in satellite imagery for each of the three steps of the transformation stage. Step 2 was characterized by an asymmetric cloud coverage, with decreased convection in the western and southern quadrants and a large area of multilayer cloud with embedded deep convection in the northern quadrant. The visible channel from the Multifunctional Transport Satellite (MTSAT) at 0359 UTC 19 September 2008, overlaid with the 85-GHz polarization corrected temperature (85PCT) imagery from the *Aqua* satellite at 0330 UTC, is shown in Fig. 3a. The 85PCT is sensitive to scattering by ice particles aloft, and is therefore representative of precipitation from about 5- to 9-km altitude. Both the visible channel and 85PCT show a highly asymmetric structure that is consistent with the characteristic signatures identified by Klein et al. (2000). The visible imagery shows a broad region of clouds to the east and northeast of the center, with the 85PCT indicating deep convective features near the center of the cloud shield. The 85PCT imagery depicts a partial eyewall that is open to the southwest and connected to a convective rainband complex to the northeast.

A composite of 36-GHz PCT (36PCT), vertically polarized (36V), and horizontally polarized (36H) channels is shown in Fig. 3b. The cyan colors depict lower-level rain and stratiform precipitation, whereas the pink colors depict upper-level ice particles and deep convection. In general, the pink, upper-level ice is displaced to the northeast of the cyan low-level rain, which is indicative of southwesterly VWS. The 36-GHz imagery also reveals differences in the structure of the eyewall at upper and lower levels. At upper levels the partial

eyewall is open to the southwest, similar to that seen in the 85PCT imagery. At lower levels the precipitation is rotated cyclonically downstream and the partial eyewall is open to the southeast.

As the satellite imagery suggests, Sinlaku was embedded in a strongly vertically sheared environmental flow. To quantify the shear magnitude and direction, the European Centre for Medium-Range Weather Forecasts (ECMWF) operational analysis at 0000 UTC 19 September 2008 was used. The 0000 UTC analysis was chosen over the 0600 UTC analysis (which is slightly closer to observation time) for shear calculations, and later on as a background state for the SAMURAI analysis, because the observed center location and vertical structure of Sinlaku was much more similar to this analysis. The horizontal mean environmental flow for each pressure level was calculated from the ECMWF analysis by averaging the meridional and zonal wind components of the grid points located within a radius of 500 km from the TC's best track center. Figure 4 illustrates that the mean environmental flow was southwesterly at all levels. The magnitude of the environmental flow up to 200 hPa steadily increases with height, from 2.7 m s^{-1} at 950 hPa to 17.1 m s^{-1} at 200 hPa. The direction of the environmental flow up to 500 hPa rotates anticyclonically with height, and from 500 to 200 hPa the direction gradually rotates cyclonically.

The vertical distribution of the horizontal mean environmental flow results in a southwesterly deep-layer shear vector (850–200 hPa) of 13.4 m s^{-1} . The robustness of the retrieved environmental flow with respect to the averaging area was tested by performing additional

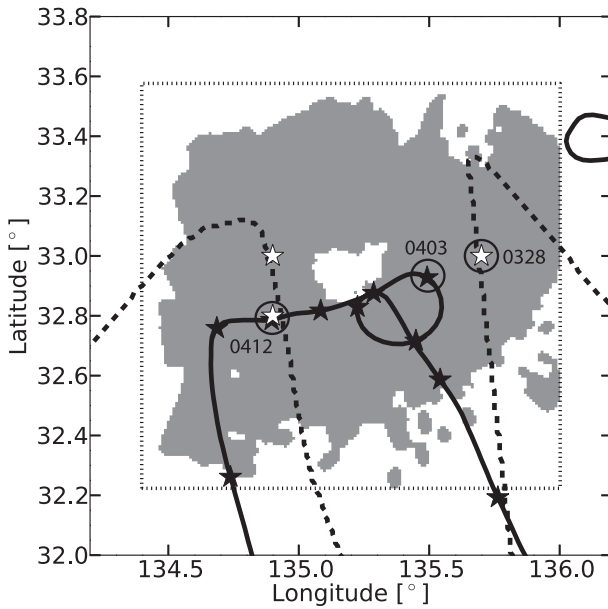


FIG. 2. Observational data used for SAMURAI input, with the dashed box defining the analysis domain. The areas where radar reflectivity and Doppler velocity were observed at 3 km is shaded gray, overlaid with the NRL P-3 flight track (solid line), USAF WC-130 flight track (dashed line), P-3 dropsonde locations (black stars), and WC-130 dropsonde locations (white stars). Soundings in Fig. 9 are circled and labeled with their release time.

retrievals for radii of 400 and 600 km. No significant sensitivities to the averaging radii were found. Additional comparisons with the Statistical Hurricane Intensity Prediction System (SHIPS) database based on the Global Forecast System (GFS) analysis were similar to the shear values calculated using the ECMWF analysis. Deep-layer shear magnitudes ranged from 13.6 to 19.7 m s^{-1} depending on the calculation method, with a similar west-southwest direction in all cases. By deep-layer shear metrics, the VWS is considered strong for a tropical cyclone and is on the upper end of climatological values found in the tropical western Pacific (Aiyer and Thorncroft 2011). The high VWS is consistent with Sinlaku's approach into the midlatitudes after recurvature, and the impending interaction with the baroclinic zone observed one day later. As will be shown later the vertical extent of the cyclonic flow was limited to approximately 9-km height; therefore, the VWS directly affecting the circulation of Sinlaku was in a shallower layer. The vertical shear in this shallower layer from 900 to 400 hPa was 7.5 m s^{-1} from the west-southwest. Shallow-layer shear from the SHIPS database is 10.2 m s^{-1} , but with a more westerly direction. A straight numerical average of the different SHIPS shear vectors yields a vector direction from 256° , which is the same direction as the shallow-layer shear vector derived

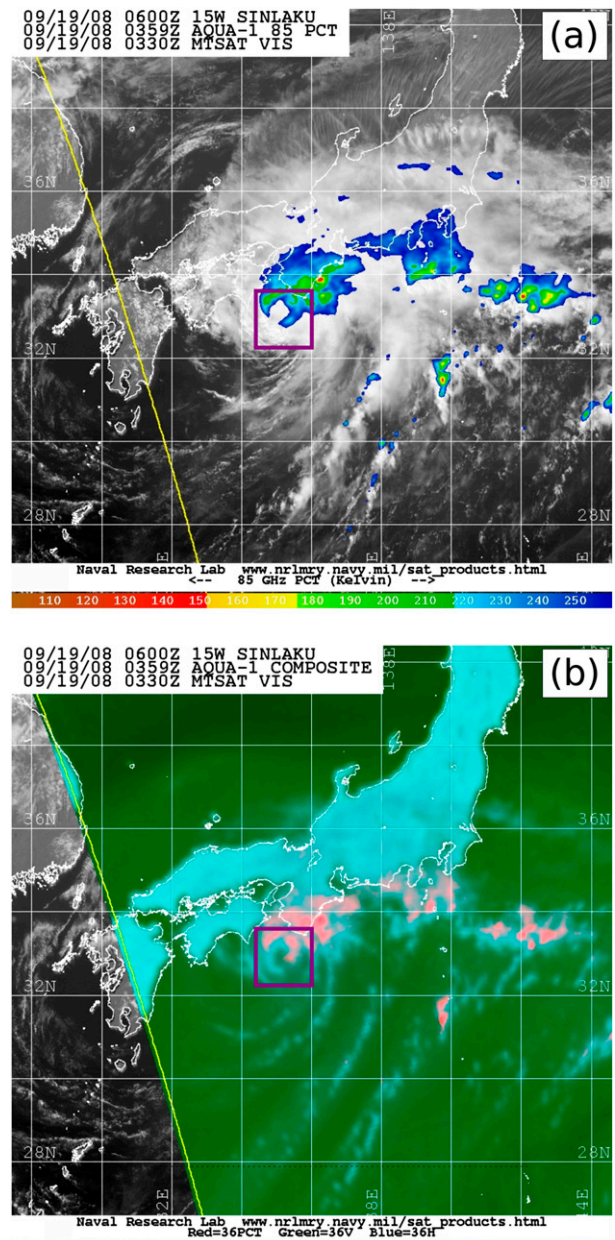


FIG. 3. (a) An 85-GHz polarization-corrected temperature image at 0359 UTC 19 Sep overlaid on a MTSAT visible image at 0330 UTC 19 Sep. (b) A 36-GHz false color composite image. The purple box indicates the radar analysis area. Satellite imagery courtesy of the Naval Research Laboratory.

from the ECMWF analysis. Therefore, the estimated shear direction appears to be robust to uncertainties in both the VWS definition and large-scale analyses. The partition into shear-relative quadrants by the different VWS definitions would be expected to change some of the details, but not the salient features of the resulting analysis.

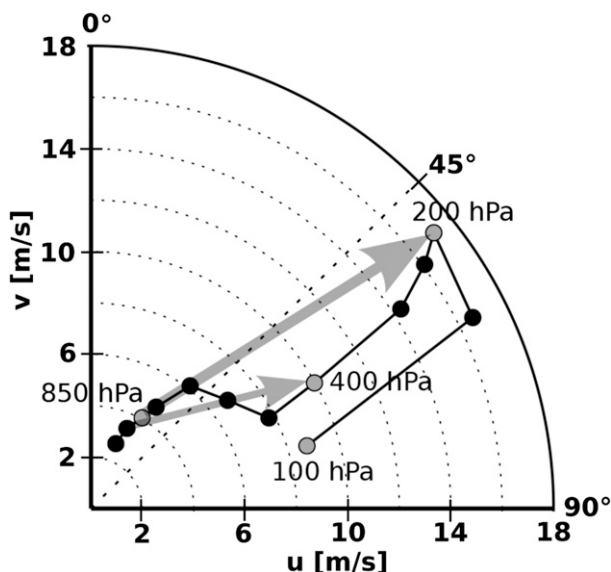


FIG. 4. Hodograph of the environmental flow derived from the ECMWF operational analysis at 0000 UTC 19 Sep. Pressure levels are 950, 900, 850, 800, 700, 600, 500, 400, 300, 250, 200, and 150 hPa. Arrows denote the deep-layer shear vector (850–200 hPa) and the shallow-layer shear vector (900–400 hPa), respectively.

b. SAMURAI methodology

The observations were analyzed using a new three-dimensional variational analysis technique called SAMURAI (Bell et al. 2012). In previous studies, mesoscale TC convective structures have been obtained by Doppler radar synthesis using Custom Editing and Display of Reduced Information in Cartesian space (CEDRIC; Mohr 1988) or variational software developed at the National Oceanic and Atmospheric Administration (NOAA) Hurricane Research Division (HRD; Reasor et al. 2009). While these tools are very valuable, they provide only kinematic analyses using radar data, and are unable to ingest additional data sources such as dropsondes, satellite vector winds, or thermodynamic data. Data assimilation packages coupled to numerical models can combine kinematic and thermodynamic measurements from different instrumentation, but they typically use strict balance constraints in order to stably integrate the primitive equations.

To bridge the gap between data assimilation and analysis, SAMURAI was developed based primarily on the work of Ooyama (1987, 2002) and Gao et al. (2004). A high-resolution analysis was performed using SAMURAI that included data from ELDORA, dropsondes, aircraft flight level, and satellite atmospheric motion vectors (Velden et al. 2005), as well as a priori background estimates from the ECMWF global analysis.

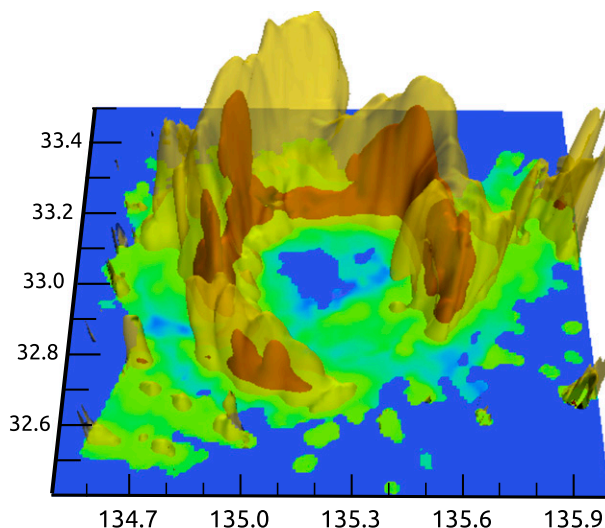


FIG. 5. Three-dimensional radar reflectivity as seen from the south. The 38-dBZ surface is shaded in red and the 28-dBZ surface is shaded in yellow. The horizontal surface is located at 1-km altitude and shaded by reflectivity with green values denoting regions with values between 10 and 20 dBZ and blue values denoting regions with <10 dBZ.

The domain size was $150 \text{ km} \times 150 \text{ km}$ from the surface to 14 km, with a horizontal node spacing of 1 km and vertical node spacing of 0.5 km. Spatial filtering was used to limit resolved wavelengths to 4 and 2 km in the horizontal and vertical directions, respectively. Additional technical details of the analysis methodology are provided in the appendix for interested readers.

3. Typhoon structure

a. Precipitation structure

The satellite imagery in Fig. 3 indicated a strong asymmetry of Sinlaku's eyewall precipitation that varied with height. A more detailed picture of the precipitation can be obtained from the ELDORA reflectivity data. To illustrate the most prominent features and provide a vertical link between the horizontal levels, a three-dimensional plot of two selected isosurfaces of radar reflectivity is shown in Fig. 5. The selected isosurfaces of 28 and 38 dBZ depict regions of moderate and heavy precipitation, respectively.

The yellow 28-dBZ surface illustrates the pronounced gap in precipitation to the southeast of the cyclone center. In the northeastern quadrant of the storm, the isosurfaces of 28 and 38 dBZ are continuous and fairly constant with azimuth, and the difference in vertical extent of the two isosurfaces is small. To the north of the center, the vertical extent of the 38-dBZ surface decreases significantly, whereas the 28-dBZ surface

reaches its overall maximum of 9-km altitude. There is a transition in the northern eyewall from the continuous 38-dBZ surface to the northeast to a more cell-like structure of the 38-dBZ surface in the western semicircle of the eyewall. Two almost vertically upright peaks of the 38-dBZ surface are apparent to the west of the center. The first peak, located just downstream of the gap to the north, exhibits the largest vertical extent of the 38-dBZ surface around the entire eyewall. The second peak, located west of the cyclone center is shallower and not as pronounced as the first one. To the southwest of the center, there are two shallow peaks of the 38-dBZ surface, disconnected from the rest of the eyewall. Overall, the strongest precipitation is predominantly located to the northeast of the center, with two regions of higher precipitation located in the western half of the eyewall. From the perspective of the VWS vector, the precipitation is strongest in the downshear direction and becomes successively weaker as one approaches the upshear direction.

A more detailed view of the reflectivity pattern along with the horizontal wind field is shown in the left panels of Fig. 6. At 1-km height (Fig. 6e, hereafter also referred to as lowest levels), the TC's eyewall is evident as a ring of high radar reflectivity. The center of the TC is located approximately at 32.9°N, 135.2°E and the radius of maximum reflectivity is approximately 35 km. The reflectivity values within the ring vary significantly with azimuth, with peak values exceeding 45 dBZ in the northeastern quadrant of the eyewall and to the southwest of the center, and values as low as 12 dBZ to the southeast of the TC center. In the northwestern quadrant of the eyewall the two peaks in radar reflectivity that were evident in the 3D plot are seen as local reflectivity maxima exceeding 45 dBZ. The maxima are suggestive of dissipating convective cells within a region of stratiform precipitation.

At 5-km height (Fig. 6c, hereafter also referred to as midlevels), the shape of the ring of highest reflectivity deviates from the shape of the ring at lower levels. The maximum reflectivity values are lower, the radial reflectivity gradients are weaker, and the ring of highest reflectivity is less circular. The maximum reflectivity values are located to the northeast of the center. To the east of the TC center, the ring of high reflectivity is wider than in other regions, and is located slightly upstream of the maximum reflectivity at lower levels. To the southwest of the TC center, where the reflectivity values at lower levels exceeded 42 dBZ, the values decrease to less than 33 dBZ. Moreover, to the southwest, the region of highest radar reflectivity seems to be located farther out from the center than elsewhere, resulting in a break in the eyewall. The gap in the eyewall reflectivity

increases in azimuth to cover most of the southern portion of the eyewall and extends further upstream compared to the gap at 1-km height. At 8-km height (Fig. 6a, hereafter also referred to as upper levels), most of the domain was covered by reflectivity values in the range of 6–21 dBZ. Three regions with values exceeding 30 dBZ were present. The maxima of radar reflectivity to the northeast and northwest were roughly collocated with the maxima at the level below, whereas the maximum to the southeast was located upstream of the broad precipitation region to the east of the center at 5-km altitude. The eyewall gap was found to the southwest of the TC center at 8 km, with reflectivity values of less than 12 dBZ. Thus, the gap continued to rotate upstream with increasing height.

A statistical comparison of the precipitation in different shear-relative quadrants is shown in Fig. 7. The quadrants are defined to be along and perpendicular to the shear vector (Fig. 6e). Tropical convection can be broadly classified into convective and stratiform components, with distinct precipitation processes and divergence profiles (Houze 1997). Yuter and Houze (1995) used contoured frequency by altitude diagrams (CFADs) to statistically describe the radar data distributions over a domain. They showed that convective regions generally display wider frequency distributions, whereas stratiform regions have much narrower distributions. Moreover, the mean radar reflectivity is generally higher in convective regions than in stratiform regions, and the vertical profile of mean radar reflectivity is different. In convective regions, the mean profile of radar reflectivity exhibits relatively constant reflectivities at lower levels and then decreases gradually toward the top. In stratiform regions, the mean profile of radar reflectivity has a sharp maximum just below the environmental 0°C level (the "bright band") and then decreases rapidly just above this level and more gradually farther above. Thus, profiles of mean radar reflectivity and standard deviation of radar reflectivity can give valuable insight into the type of precipitation.

The mean reflectivity is shown in Fig. 7a, indicating the highest values are found in the low-level upshear left (UL) quadrant. Low-level reflectivity is similar in the downshear left (DL) and upshear right (UR) quadrants, but the DL quadrant has higher reflectivity aloft. The mean reflectivity is weakest in the low-levels of the downshear right (DR) quadrant. DR reflectivity is higher aloft as a result of the elevated maximum seen in Figs. 5 and 6. The standard deviation of reflectivity in each quadrant is shown in Fig. 7b. Although the mean value is a maximum at low-level UL, the standard deviation is small in this region suggesting mostly

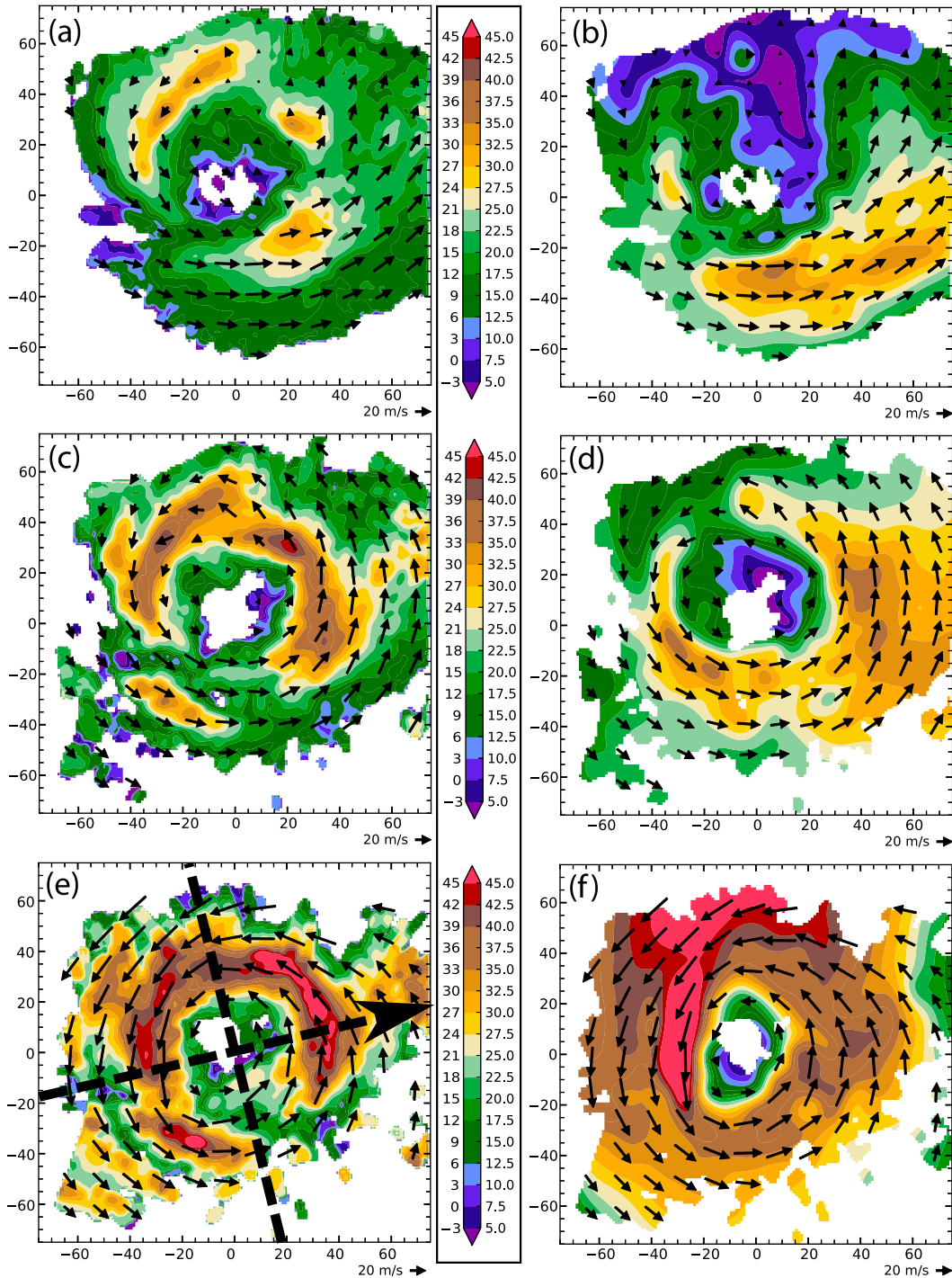


FIG. 6. (a),(c),(e) Radar reflectivity in dBZ and (b),(d),(f) storm-relative wind speed in m s^{-1} with horizontal wind vectors: (a),(b) 8-, (c),(d) 5-, and (e),(f) 1-km altitude. The vertical shear vector and the partition of the domain into shear-relative quadrants are shown in (e).

stratiform precipitation. Higher standard deviations aloft compared to the other quadrants are associated with the two maxima presumed to be dissipating convective cells. The highest standard deviation is found at

low-level DL, consistent with the deep convective activity in this region. The UR standard deviation is similar to that found UL, suggesting a similar type of precipitation at low- to midlevels. Convection in the DR

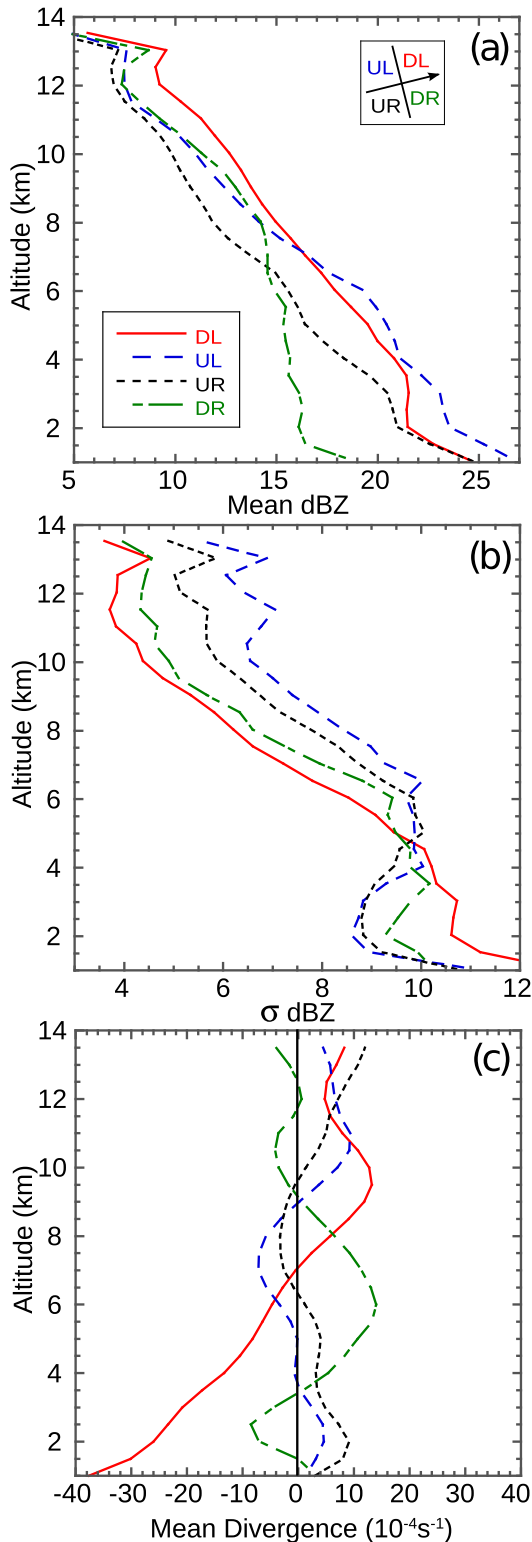


FIG. 7. (a) Mean radar reflectivity (dBZ), (b) its standard deviation (dBZ), and (c) mean divergence ($10^{-4} s^{-1}$) vs altitude for downshear left (red solid line), upshear left (blue dashed), upshear right (black dotted), and downshear right (dot dashed) quadrants.

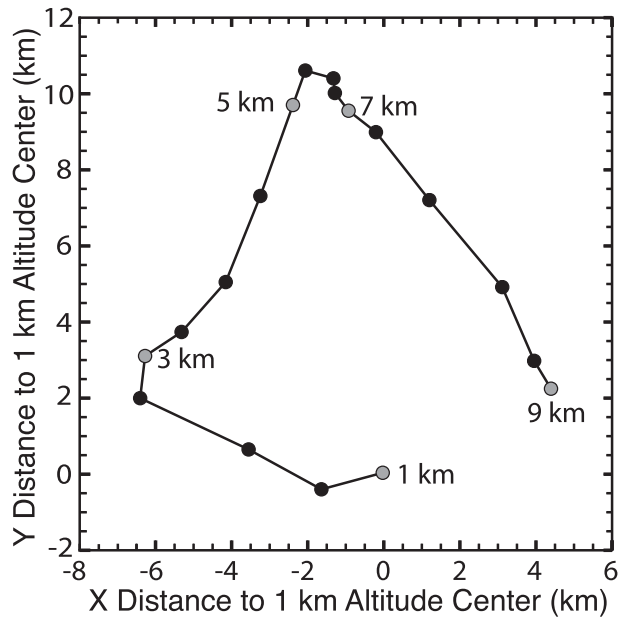


FIG. 8. Circulation center locations from 1- to 9-km altitude in 0.5-km increments.

quadrant has an intermediate standard deviation, consistent with the variety of weak echoes in that region.

b. Kinematic structure

VWS results in a tilt of the vortex in the vertical. This tilt may process and change its magnitude over time, allowing the vortex to develop resiliency to shear (Jones 2004). Mostly the vortex tilt is found to be directed somewhat downshear left (e.g., Reasor et al. 2004; Reasor and Eastin 2012). To assess the tilt of Sinlaku, the vortex center at different levels was determined using the simplex method described by Marks et al. (1992). They define the center as the point where the mean tangential wind in a given annulus is maximized. The method was found to be robust for vortices in shear (Reasor and Eastin 2012). The simplex method produces good results up to 9 km in Sinlaku, but above that level the cyclonic circulation was relatively weak and the center became ill defined. The center positions for the lowest 9 km (Fig. 8) show an anticyclonic rotation with height consistent with the anticyclonic rotation of VWS (Fig. 4). As for the VWS calculation, the tilt direction and magnitude depend on the levels that are used to compute them.

Horizontal wind speed is shown in the right panels of Fig. 6. Recall that the analysis was performed in a storm-relative framework, so the motion asymmetry seen in an earth-relative framework has been removed. At 1-km height (Fig. 6f), the shape of the wind speed distribution is elliptic, in contrast to the more circular shape of the

reflectivity distribution. The ellipticity may be due to the presence of an azimuthal wavenumber two vortex Rossby wave propagating on the azimuthal mean vorticity gradient (Montgomery and Kallenbach 1997; Lee et al. 2006). The presence of a wavenumber-2 perturbation is consistent with the barotropically unstable ring vorticity structure (shown in Fig. 10), and also with the VWS tilt-induced asymmetries (Reasor et al. 2004).

The highest wind speeds, exceeding 45 m s^{-1} , are located in the western eyewall and extend toward the north of the TC center into a broad region of high winds located near the 50-km radius. The location of highest wind speeds does not coincide with the location of the highest low-level radar reflectivity, but is rather collocated with the mixed convective-stratiform portion of the eyewall in the UL quadrant. We speculate that this maximum is due to a combination of descending midlevel inflow from the stratiform elements and low-level vortex stretching from the convective elements in this quadrant (Hence and Houze 2008), but a detailed tangential wind budget is beyond the scope of this study. The lowest wind speeds within the eyewall are located to the south of the center, with values near 35 m s^{-1} . The lower wind speeds in this region are consistent with the lack of convective activity.

The horizontal winds at 5-km height are still cyclonic, but the wind maximum has shifted to the southern quadrants (Fig. 6d). This shift is consistent with the increasing magnitude of the environmental west-southwesterly flow impacting the weaker TC circulation. To the east and southwest of the storm center, the wind speed exceeds 35 m s^{-1} . To the northwest of the center the wind speed is as low as 20 m s^{-1} , resulting in a strong vertical gradient of wind speed in this region. At 8-km height (Fig. 6b), the wind speed shows a dominant wavenumber-1 pattern, with high wind speeds to the southeast of the TC center and low wind speeds to the northwest. The wind speed to the north of the center is almost zero, suggesting that the strong environmental flow was approximately the same magnitude as the cyclonic flow at this altitude. At levels slightly higher than 8 km, the cyclonic circulation was no longer closed in the storm-relative frame of reference.

The mean divergence in each shear-relative quadrant is shown in Fig. 7c. Convective and stratiform precipitation have distinct signatures in their divergence profiles in addition to distinct signatures in radar reflectivity. Convective regions show convergence at low levels and divergence aloft, while stratiform regions show convergence at midlevels with divergence above and below (Houze 1997). The change in divergence profiles is due to a decrease in active, vigorous convection and a transition from warm-rain-dominated

microphysics to predominately ice-phase microphysics. There is a clear convective signal in the downshear quadrants, with convergence at low levels and divergence aloft. The convergence was the strongest and deepest in the DL quadrant, consistent with the nearly contiguous band of deep convection in this region. Weaker convergence and a lower divergence maximum near 6-km altitude is found DR. The upshear quadrants have a more stratiform profile, with low-level and upper-level divergence and midlevel convergence. The UL quadrant had a slightly stronger midlevel convergence maximum, while the UR quadrant had a slightly stronger low-level divergence maximum.

A sounding taken in the UR quadrant (Fig. 9a) provides some corroborating observations of stratiform precipitation and maturing convection in that region (all sounding locations are indicated by the stars in Fig. 2). The sounding is nearly saturated and moist adiabatic above 850 hPa, but shows a distinct warming between 850 and 950 hPa, with an inversion and dry adiabatic lapse rate below 950 hPa. The thermodynamic profile is consistent with the presence of a low-level downdraft that is evaporatively cooled above 850 hPa, followed by a layer of dry subsidence warming atop a shallow mixed layer at 950 hPa (Zipser 1977). In contrast, a sounding taken in the eastern part of the eyewall (DL) exhibits deep saturated conditions (Fig. 9b), as expected for a typical eyewall sounding consisting primarily of an updraft. The limited dropsonde sampling (Fig. 2) precludes a detailed comparison of thermodynamics in the other eyewall quadrants.

Figure 10 shows the vertical vorticity (left panels) and vertical velocity (right panels). A ring of positive vorticity near the 20-km radius is evident at 1 km (Fig. 10e) with values exceeding $3.75 \times 10^{-3} \text{ s}^{-1}$. To the west, there is a small strip of negative vorticity outside the region of strongest positive vorticity due to the strong radial shear of the tangential wind in this region. The ring structure is still evident at 5-km altitude (Fig. 10c), but with more localized maxima. As the wind speeds decrease with height, the vorticity also decreases and transitions from a ring to a more cellular structure.

The interpretation of the vertical velocity in Fig. 10 is on the relative magnitudes and patterns of mesoscale ascent and descent, with less emphasis on the absolute values. Uncertainty in vertical velocity is introduced by several sources such as assumptions about the size distribution of the scattering particles and their fall speed, the geometry of the scanning beams, and the spatial filtering used in the analysis (Matejka and Bartels 1998). At 1-km altitude (Fig. 10f), a small region of ascent is located to the southwest of the center, with a broad region of ascent to the northeast. At 5-km altitude (Fig. 10d),

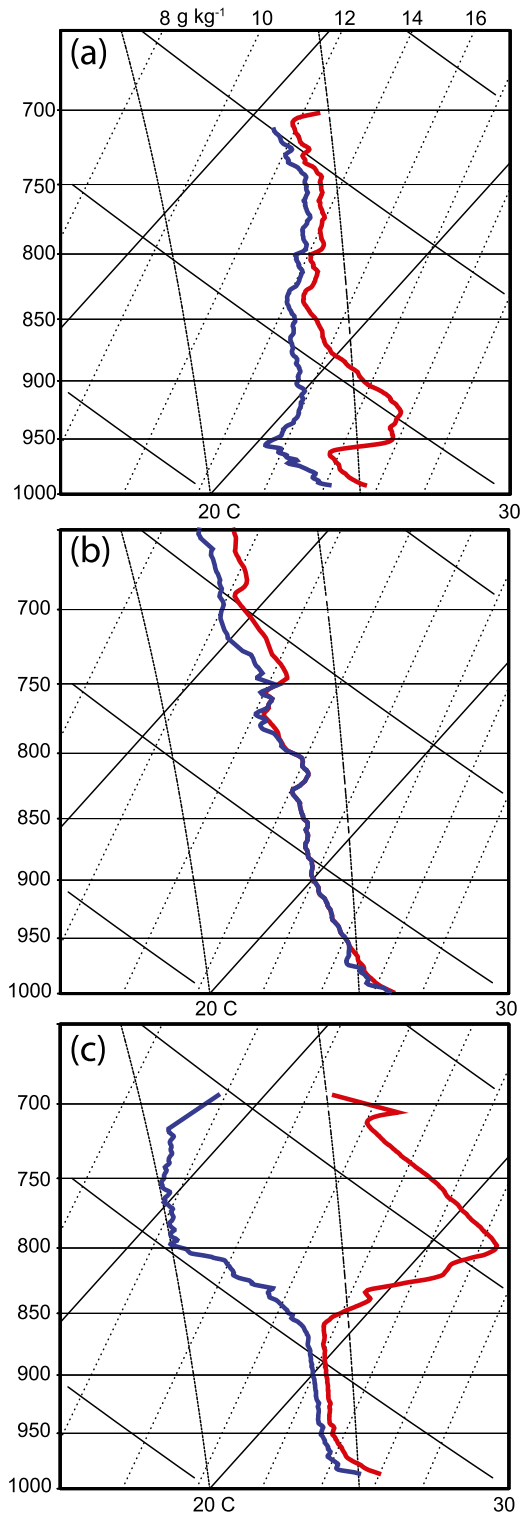


FIG. 9. Skew T - $\log p$ soundings with the red line denoting temperature and blue line denoting dewpoint temperature. Soundings are from the (a) upshear right quadrant at 0412 UTC, (b) downshear left quadrant at 0328 UTC, and (c) eye at 0403 UTC. The sounding launch locations are marked in Fig. 2.

an open ring of upward motion extends from the southeast to northwest, consistent with the midlevel reflectivity pattern. This updraft ring is flanked on both sides by downward motion, with the strongest regions of descent occurring on the inside edge of the eyewall, especially to the west of the center. At 8-km altitude (Fig. 10b), the updraft ring is still apparent, and is displaced radially outward from lower levels indicating an outward-sloping updraft. Stronger descent than that seen at 5 km is found outside the updraft ring, with three local maxima radially inside the eyewall. In vertical cross sections shown later, it can be seen that the inner region of downward motion to the northwest of the center indicates air cascading down the inner edge of the eyewall. Weaker downward motions are found radially outside the band of upward motion to the southeast of the center.

A statistical comparison of the vertical velocity in the shear-relative quadrants is shown in Fig. 11. The analysis is displayed by vertical-mass-flux-weighted CFADs of vertical velocity [i.e., the vertical velocity was binned in 1 m s^{-1} intervals in each quadrant and then weighted by the air density, the vertical velocity and the area of a grid cell (1 km^2) at each vertical level]. The vertical gradient of vertical mass flux is directly related to the divergence of the horizontal wind field. The differences between the quadrants are striking with this visualization, illustrating the strong asymmetry in vertical motion by quadrant. The upward mass flux in the DL quadrant is a dominant feature, with two low-level maxima exceeding $1.5 \times 10^9 \text{ kg s}^{-1}$ associated with 1 and 2 m s^{-1} updrafts. A secondary upward maximum is evident at 7-km altitude, possibly due to added buoyancy from the latent heat of freezing. Very little downward mass flux was seen in the DL quadrant. The CFAD UL suggests a more even distribution of mass flux, but with a higher frequency of downdrafts. In the UR quadrant downward mass flux exceeded 10^9 kg s^{-1} near 3-km altitude that was associated with 1 m s^{-1} downdrafts. A non-negligible low-level upward mass flux was also found in the UR quadrant that was associated with the convective feature displaced from the eyewall. In the DR quadrant, an upper-level downward mass flux was seen, along with weak upward mass flux at midlevels. The CFADs encompass both the newly forming cells and cloudy downdrafts in this region, reducing the peaks in the frequencies. Since, in saturated conditions, the vertical mass flux is proportional to latent heating and cooling, the CFAD visualization can be seen as a proxy for latent heating in the different storm quadrants and altitudes, and can also identify the predominant vertical velocities accomplishing the heating (Houze et al. 2009).

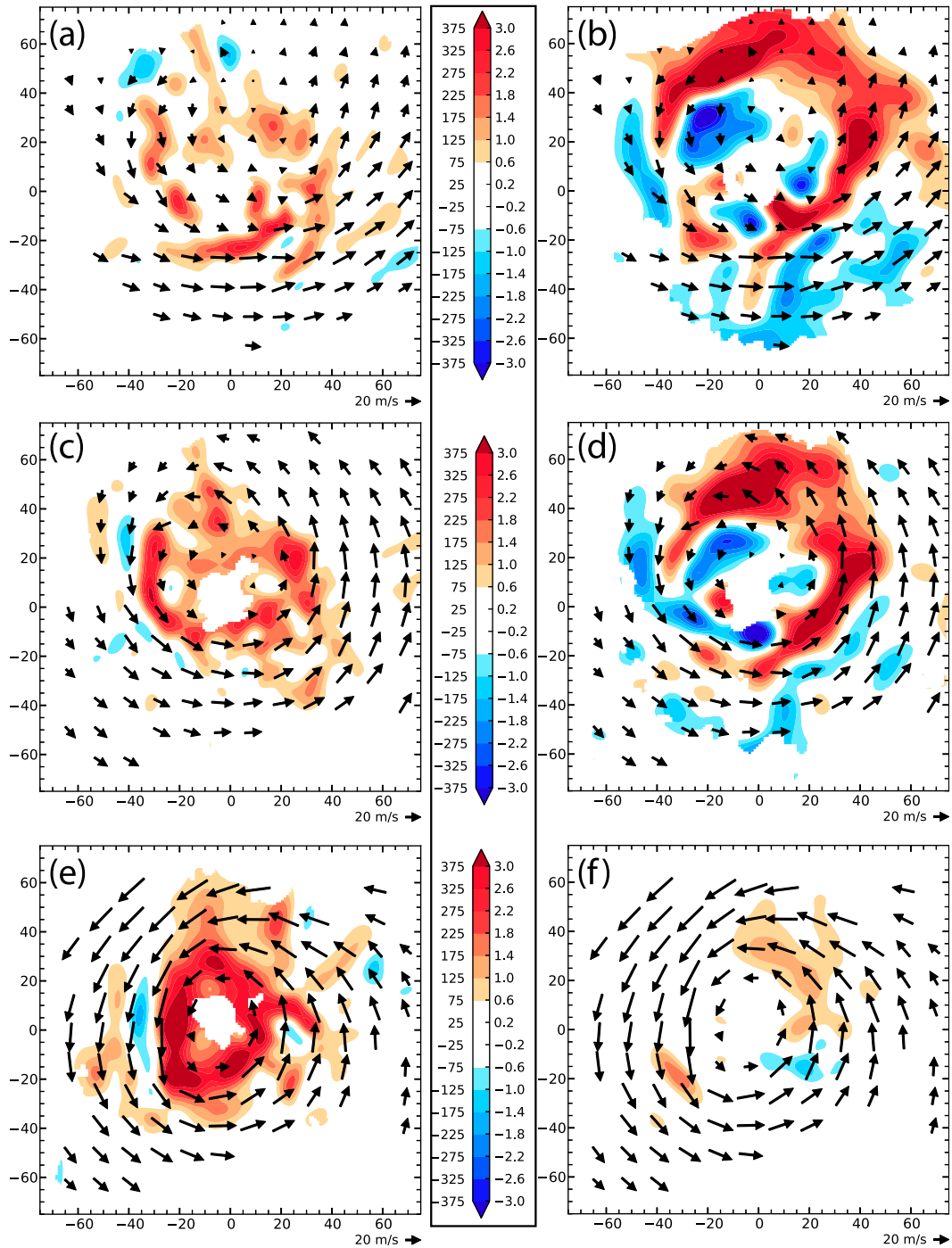


FIG. 10. (a),(c),(e) Vertical vorticity in 10^{-5} s^{-1} and (b),(d),(f) vertical velocity in m s^{-1} with horizontal wind vectors: (a),(b) 8-, (c),(d) 5-, and (e),(f) 1-km altitude.

In general, the CFADs are consistent with the maturing convection as one travels cyclonically around the vortex. The downward mass flux steadily increases in both magnitude and depth cyclonically from DL to UR. A similar transition is seen in the upward mass flux from DR to DL, with a secondary maximum UR associated

with the displaced convective feature. The CFADs suggest that strong low-level latent heating in the convectively active DL quadrant transitions to an increased dominance of low-level evaporative cooling downstream as the convection matures. The reflectivity structure, convergence and mass flux profiles, and eyewall soundings

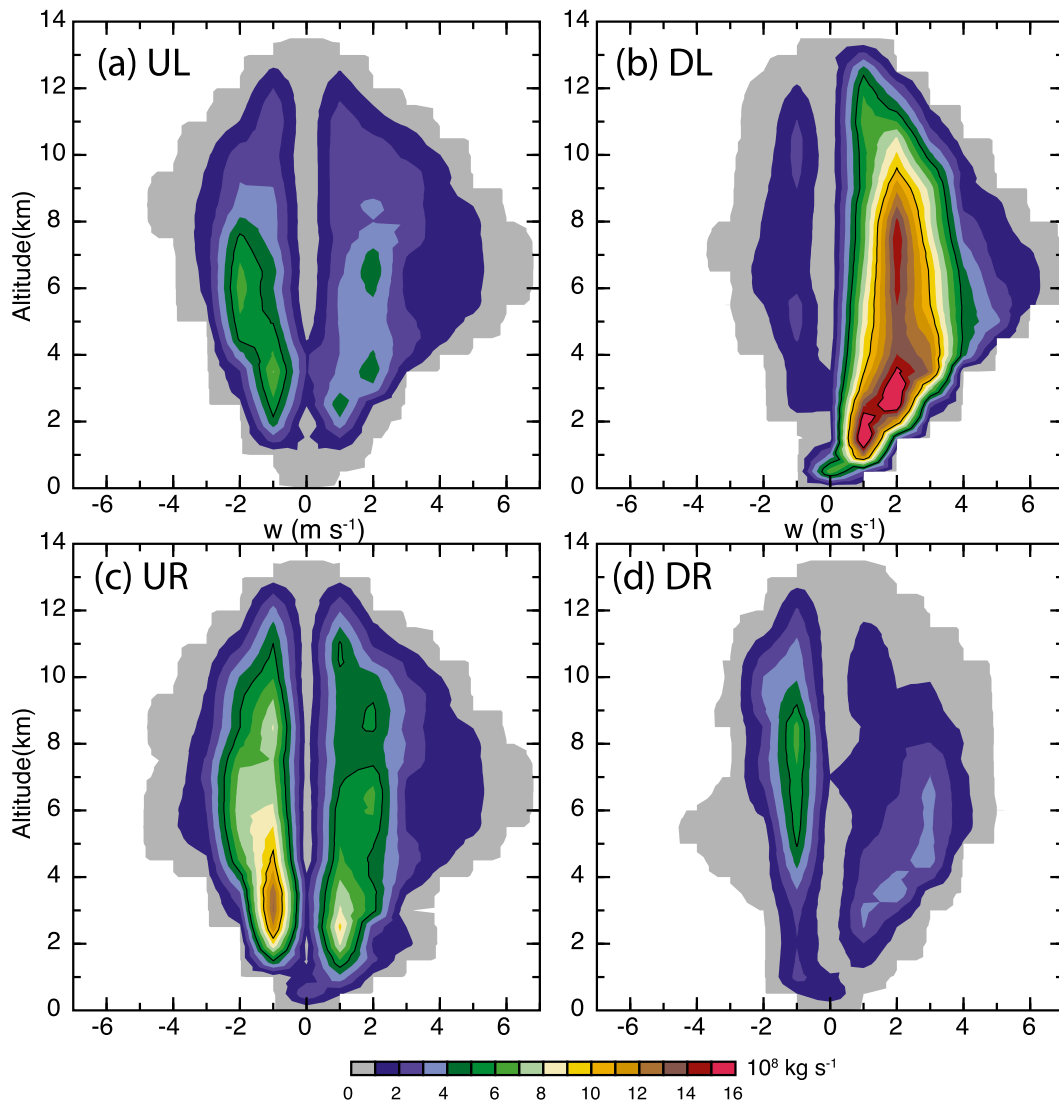


FIG. 11. Vertical-mass-flux-weighted CFADs of vertical velocity for each shear-relative quadrant. The CFADs show the frequency of vertical velocities in 1 m s^{-1} increments occurring at different altitudes, with the frequency weighted by vertical mass flux $\rho w A$, where ρ is the air density, w is vertical velocity, and A is the area of a grid cell (1 km^2). The contour units are 1×10^8 with the 1×10^9 and $1.5 \times 10^9 \text{ kg s}^{-1}$ contours highlighted.

are all consistent with the interpretation of a convective to stratiform transition occurring downstream of the DR quadrant.

Vertical cross sections provide further insight into the convective transition around the eyewall by combining the kinematic and precipitation features. Figure 12 shows the radar reflectivity in color, tangential wind in contours, and secondary circulation in vectors through each of the four shear quadrants. Starting in the DR quadrant (Fig. 12d), the elevated reflectivity maximum believed to be associated with convective initiation is evident, coincident with an outward-tilted updraft. Radial winds were generally outward, but convergence and

storm-relative inflow can be seen below 4-km altitude. Tangential winds were largest at low levels, and were elevated in the updraft due to vertical advection.

Strong low-level convergence was present in the DL quadrant (Fig. 12b), with a broad tilted updraft originating below 2-km altitude. The precipitation in the eyewall was nearly upright, with heavy rain at the base of the eyewall. The vortex tilt is evident in the upper-level tangential winds, as the zero isotach moves radially outward with height and anticyclonic winds (with respect to the low-level center) can be seen in the upper-level eye. Weak descent is evident inside the eye that is consistent with the lack of precipitation in that region.

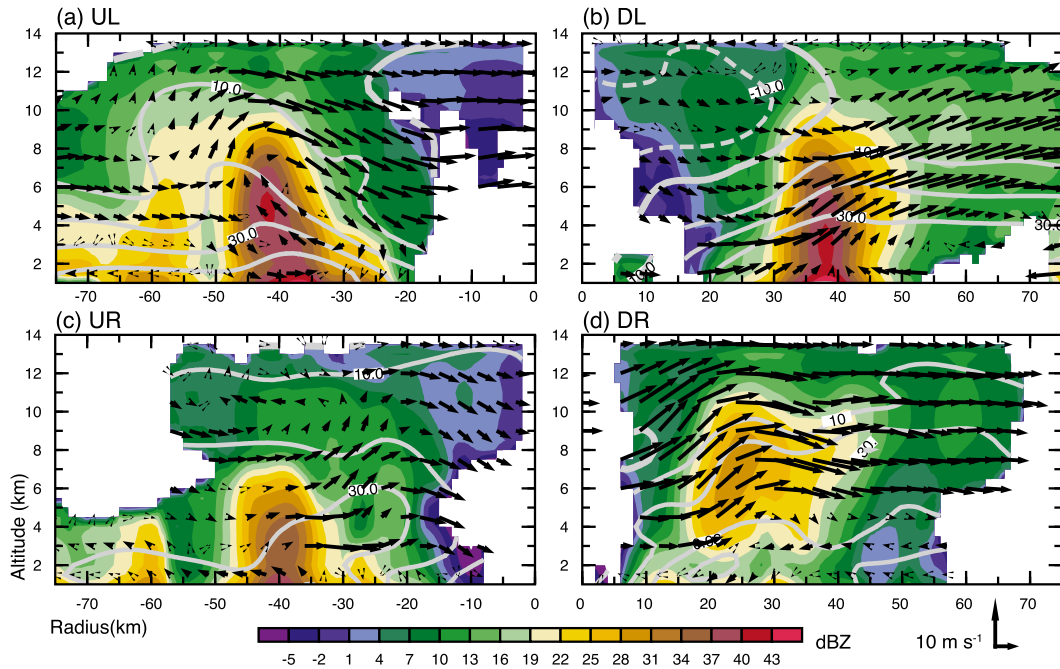


FIG. 12. Vertical cross sections of radar reflectivity in dBZ (shaded), tangential wind in m s^{-1} (gray contours), and in-plane wind vectors composed of radial and vertical velocity for each shear-relative quadrant. Cross sections are taken from the corner of the domain to the center, 45° from the x and y axes in each quadrant: (a) upshear left, (b) downshear left, (c) upshear right, and (d) downshear right.

Radar reflectivity was still strong in the UL quadrant (Fig. 12a), but with a more outward tilt to the eyewall. An outward tilt was also evident in the tangential winds. Midlevel inflow was coupled to an upper-level updraft and lower-level downdraft on the outside edge of the eyewall in this quadrant, consistent with the presence of stratiform precipitation (Moon and Nolan 2010). A low-level tilted updraft is evident in the strongest reflectivity in the eyewall, with low-level convergence at the leading edge of the reflectivity maximum. A maximum in low-level tangential winds and vertically distorted isotachs are collocated with the descending midlevel inflow flanked by the eyewall updraft. The secondary circulation resembles that of a tropical squall line, with the deeper convection flanked by a trailing stratiform region. We speculate that this convective arrangement may have been responsible for the maximum low-level winds in this quadrant.

The high sensitivity of ELDORA reveals that deep-layer descent was maximized on the inside edge of the eyewall in the UL quadrant. No sounding was released in this area, but an eye sounding on the inside edge of the downshear side of the eyewall is shown in Fig. 9c. A shallow, moist layer is evident that was topped by a 3.5-K temperature inversion and 6-K dewpoint depression, consistent with the presence of strong descent and subsidence warming. Other thermodynamic soundings

across the eye (not shown) are similar to the one in Fig. 9c, but with varying depth of the moist layer and strength of the inversion. The eye soundings are similar to those seen in other tropical storms (Willoughby 1998), providing evidence that the cold-core transition had not yet taken place.

Farther downstream, the reflectivity and vertical velocity were weaker in the UR quadrant (Fig. 12c). Inflow was strongest at midlevels, and the upper-level inward tilted updraft was associated with slightly elevated reflectivity aloft. No significant updraft can be seen in the shallow eyewall feature, and the lighter precipitation and vertical velocity are consistent with decaying convection and predominately stratiform precipitation in this region. The isotachs of the tangential wind tilted slightly inward here, in contrast to the other three quadrants but consistent with an inward and upward advection of tangential wind in this region. Deep-layer descent was found inside the eye similar to that seen in the UL quadrant.

c. Thermodynamic structure

Drosondes released in Sinlaku's inner core presented above suggest that the eyewall consisted of a nearly saturated updraft in the DL quadrant, had strong subsidence warming and a low-level inversion across the eye, and revealed the presence of moist

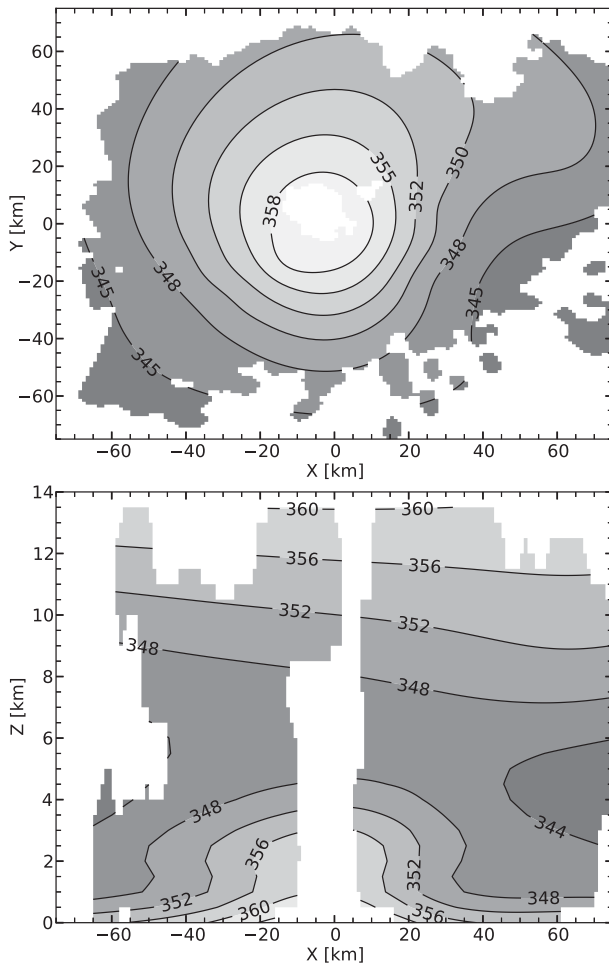


FIG. 13. (top) Horizontal cross section of equivalent potential temperature θ_e at 2-km altitude and (bottom) a vertical west-east cross section of θ_e cutting through the center of the storm. For consistency with the radar analysis, the data are masked where there are no reflectivity data.

downdrafts in the UR quadrant. The dropsonde coverage was rather sparse (Fig. 2), so details in the thermodynamic field may be under-resolved. Nevertheless, a few interesting, broader features can be identified from the SAMURAI analysis of the equivalent potential temperature (θ_e) structure (Fig. 13). Areas without radar reflectivity were removed from the plot for easier comparison with the radar-derived structures shown previously. Despite Sinlaku's proximity to the mid-latitudes, and in contrast to storms undergoing extratropical transition, no frontal structure was present in the core region of the storm. The storm still possessed a relatively symmetric thermodynamic structure and had a shallow warm core, consistent with step 2 of the transformation stage. Figure 13 (top) indicates decreasing θ_e values with radius at 2-km altitude, with a maximum of over 358 K at the center of the storm

decreasing to below 345 K at the outer edge of the SAMURAI domain. The warm core extends up to a height of about 5 km (Fig. 13, bottom). A midlevel θ_e minimum is evident at 60-km radius, suggesting the presence of drier, cooler air outside the eyewall. The relatively symmetric thermodynamic structure was replaced by a more frontal structure 24 h later as interaction with the baroclinic zone commenced.

4. Discussion

The preceding analysis has focused on VWS as a primary influence in determining the eyewall structure during the extratropical transformation stage. There are other factors that may have influenced the inner-core structure of Sinlaku such as storm motion, dry environmental air, sea surface temperature, the higher-latitude environment with its increased baroclinicity, and proximity to land. In contrast to other cases where the poleward-moving storm strongly interacts with and alters the midlatitude flow (Atallah and Bosart 2003; Harr et al. 2008; Anwender et al. 2008; Agusti-Panareda et al. 2004), no such interaction could be identified for Sinlaku at this time. The thermodynamic structure does not suggest that environmental baroclinicity had begun to play an important role at this stage. The location just south of Japan suggests an orographic contribution may have aided ascent of the onshore winds located to the east of the center of Sinlaku and descent of the offshore winds located to the west of the center. The locations of forced ascent and descent by orography are therefore at the same locations as the VWS-induced ascent and descent. The orography may have slightly enhanced the shear-induced flow pattern of upward motion on the downshear side and downward motion on the upshear side. But since the asymmetric pattern of eyewall convection did not change significantly as Sinlaku approached Japan, we assume that orography only had a minor effect on the flow pattern compared to the VWS.

One limitation of our study is the inability to document the temporal evolution of the eyewall structure (e.g., to document the life cycle of individual cells as they travel around the eyewall), because of the limited aircraft flight duration. A detailed comparison with the findings of previous case studies by Black et al. (2002), Reasor et al. (2009), and Reasor and Eastin (2012) helps to provide insight into the temporal evolution of eyewall convective cells in VWS and put the observed structure of Sinlaku into broader scientific context.

Black et al. (2002) studied eastern Pacific Hurricanes Jimena (1991) and Olivia (1994). Hurricane Jimena was observed on two consecutive days. On the first day,

TABLE 1. Mean values of latitude, wind speed, central pressure, and Reynolds sea surface temperature (RSST) averaged over the observation periods for Jimena (1991), Olivia (1994), Guillermo (1997), and Sinlaku (2008). RSST data are taken from the SHIPS database; all other variables are from best track data from NHC (Jimena, Olivia, Guillermo) and JTWC (Sinlaku).

Storm	Ocean basin	Lat ($^{\circ}$ N)	Wind [kt (m s^{-1})]	Pressure (hPa)	RSST ($^{\circ}$ C)
Jimena	East Pacific	13.4	114 (59)	947	29.0
Olivia	East Pacific	17.5	115 (59)	936	27.8
Guillermo	East Pacific	13.6	123 (63)	937	29.5
Sinlaku	West Pacific	33.0	68 (35)	972	28.0

23 September 1991, Jimena was exposed to nearly constant easterly shear and maintained a near-constant intensity. The maximum VWS was 20 m s^{-1} between 1- and 10-km altitude and the maximum wind speed was 57 m s^{-1} . A plan position indicator (PPI) radar composite showed asymmetries in the reflectivity, with higher values ($>45 \text{ dBZ}$) left of shear and lower values ($<35 \text{ dBZ}$) right of shear. These reflectivity magnitudes and pattern are consistent with those observed in Sinlaku. Jimena's general reflectivity pattern persisted throughout the 3 h of observations, but the reflectivity was not a steady feature. Sweep-by-sweep images showed that cells generally first appeared in the downshear direction and traveled cyclonically downstream at approximately 60% of the wind speed at the RMW. Most cells dissipated in the upshear semicircle after traveling $\sim 135^{\circ}$, and only one cluster of cells circled the eye twice. The vertical velocity showed localized updrafts on the downshear side and downdrafts beneath upper-level, glaciated updrafts on the upshear side. The structure of Sinlaku also transitions from deeper, stronger updrafts on the downshear side to upper-level updrafts and low-level downdrafts associated with stratiform precipitation on the upshear side.

Hurricane Olivia was also observed on two consecutive days. On the second day, 25 September 1994, Olivia weakened as westerly shear increased and the TC moved into a region of cooler sea surface temperatures. The observation period lasted for 4 h. In the beginning, the vertical shear was only 3 m s^{-1} , but increased to about 15 m s^{-1} over the course of time. PPI composites indicated an increasingly asymmetric structure of the eyewall and a change in the lifetime of the cells. In the beginning, the eyewall contained many persistent radar echos that circled the eye completely at 80%–90% of the speed at the RMW. As the VWS increased, the lifetime of the cells decreased to 5–10 min and the high reflectivities became increasingly confined to the left-of-shear octant, although the greatest reflectivities in the PPI composites increased slightly.

Reasor and Eastin (2012) used radar and flight-level data of Hurricane Guillermo from two observation periods on two successive days. On 2 August 1997, Hurricane Guillermo rapidly intensified in increasing

deep-layer VWS of about 8.5 m s^{-1} . On 3 August 1997, Hurricane Guillermo exhibited constant intensity in decreasing VWS of about 4 m s^{-1} . The difference in VWS on these two days was reflected in the structure of the eyewall convection of Hurricane Guillermo. During the first observation period the eyewall reflectivity showed a pronounced convective asymmetry, with the largest reflectivity values in the left of shear semicircle. During the second observation period, the eyewall reflectivity structure was considerably more symmetric.

These previous studies of Hurricanes Jimena, Olivia, and Guillermo show a consistent picture of the qualitative effects of VWS on the eyewall convection. New cell formation occurs somewhat upstream of the downshear direction and after maturing a little bit they are detected by the radar in the downshear direction. The highest radar reflectivities are located to the left of the VWS vector, and the weaker the shear the farther the convective cells circle around the eye. Although the dataset of Sinlaku did not allow us to track individual cells throughout their life cycle as was done in the previous studies, the very close resemblance to their findings suggests that the snapshot picture of Sinlaku's structure with strong convection downshear and stratiform convection upshear is also representative of the life cycle of individual cells.

In contrast to Jimena, Olivia, and Guillermo, Sinlaku was located much farther north and was much less intense (see Table 1). At analysis time, Sinlaku was located at 33° N, whereas the referenced storms were all located well south of 20° N. Nevertheless, the sea surface temperatures in Sinlaku still reached 28.0° C. Sinlaku was located in the western Pacific, whereas Jimena, Olivia, and Guillermo were located in the eastern Pacific. Sinlaku had surface wind speeds of 35 m s^{-1} and a central pressure of 972 hPa, whereas the referenced storms had wind speeds in excess of 55 m s^{-1} and central pressures lower than 950 hPa. Despite the differences in environments and intensity, Sinlaku's eyewall structure looked strikingly similar to these other cases. These similarities in the eyewall structure of Sinlaku to the structure of these other cases emphasize the importance of shear on the inner-core dynamics. Moreover, it supports the hypothesis of Klein et al. (2000) and Ritchie

and Elsberry (2001) that vertical wind shear is the primary factor influencing the TC structure during step 2 of the transformation stage of extratropical transition. Thus, before the inner core region of the TC interacts with the baroclinic zone itself, the increased proximity to the baroclinic zone manifests itself primarily by imposing increased vertical wind shear on the TC inner core circulation.

The excellent ELDORA coverage of the entire eyewall, in combination with the new SAMURAI data analysis tool, enabled a detailed analysis of the characteristics of the eyewall convection. The precipitation and convergence profiles for the different quadrants revealed a strong resemblance to the structure of principal and secondary rainbands (Barnes et al. 1983; Didlake and Houze 2013a,b), with a transition from convective to stratiform precipitation downstream. Thermodynamic measurements from dropsondes are also consistent with the convective to stratiform transition. While downstream stratiform precipitation appears to have been observed in the previous case studies, the link between eyewall and rainband structure was not explicitly made. The more prominent stratiform region in Sinlaku compared to previous sheared storms may partly be due to its reduced intensity. Slower advective speeds may allow for longer cell lifetimes and enhanced stratiform precipitation processes in the eyewall that are more similar to rainbands in more intense TCs. The similarity of these structures suggests that the distinction between eyewall and rainband may be less sharp than previously thought, and their convective response to VWS may be similar.

Besides altering the structure of the eyewall convection directly, other mechanisms have been proposed that would lead to weakening due to vertical wind shear. Riemer et al. (2010, 2013) recently proposed that vertical wind shear results in a flushing of the inflow layer by low entropy air. Downdrafts associated with a wavenumber-1 convective asymmetry outside the eyewall, forced by the tilt of the outer vortex, can import low entropy air into the boundary layer. This low entropy air in the storm's inflow layer diminishes the energy supply for the convection and may therefore weaken the storm's circulation. Satellite imagery (Fig. 3) shows that there was an extensive region of convection just outside of the SAMURAI domain to the northeast of the center. Only limited dropsondes were released in this region and therefore it is beyond the scope of this study to test the VWS effect suggested by Riemer et al. (2010).

Another important result is that the strongest low-level inflow and convergence was found downshear, but mid-level inflow and convergence became prominent upshear. The low-level inflow maximum downshear was also

observed in the shear composite by Reasor et al. (2013), but a midlevel inflow maximum was not reported. Midlevel eddies induced by VWS were proposed by Tang and Emanuel (2010) as a mechanism for reducing TC intensity through direct ventilation of the eyewall convection by low-entropy air. In addition to ventilation by vortex asymmetries, we hypothesize that the midlevel inflow driven by stratiform precipitation processes may have played a role in extratropical transition to a cold core system. Midlevel inflow can efficiently converge angular momentum into the eyewall above the boundary layer and intensify the midlevel circulation (Smith et al. 2009), but it can also directly import the low-entropy air from outside the eyewall and weaken the deep convection (Didlake and Houze 2013b). The balanced thermal response to a midlevel circulation is a cold-core system (Raymond and Jiang 1990), suggesting that the stratiform portion of the eyewall may facilitate the extratropical transition by strengthening the midlevel circulation and ventilating the eyewall convection.

Overall, the very close resemblance of the eyewall structure of Sinlaku with the structure of mature storms in VWS strongly suggests that vertical shear dynamics were more important than baroclinic impacts at this time, consistent with the conceptual model of Klein et al. (2000). No evidence of frontal structure was present, and the TC was still warm cored during the observation period. The observation period took place right before the final weakening of Sinlaku. The next detailed view of the inner core region of Sinlaku was available 24 h later. Interaction with the baroclinic zone resulted in significant changes in the kinematic, thermodynamic, and precipitation structure such as warm and cold frontal structures and an intrusion of drier midlatitude air. A detailed analysis of that period is presented in a companion paper (Quinting et al. 2014).

5. Summary and conclusions

Mesoscale observations of Typhoon Sinlaku were collected as part of the T-PARC/TCS08 field campaign as the TC recurved into the midlatitudes. Two simultaneous flights into Sinlaku on 19 September documented the structure of the typhoon after a period of reintensification and during step 2 of the transformation stage of extratropical transition as defined by Klein et al. (2000). Detailed observations of a TC in this late stage of its life cycle are very rare and offer a unique opportunity to examine the eyewall structure of a transitioning typhoon. Doppler radar, dropsondes, aircraft in situ data, and satellite atmospheric motion vectors were combined into a high-resolution analysis of the

inner core region using a new variational analysis technique called SAMURAI. Three-dimensional kinematic and precipitation fields with a 1 km horizontal and 0.5 km nodal spacing reveal an asymmetric eyewall structure that is generally consistent with known impacts of vertical wind shear.

Klein et al. (2000) and Ritchie and Elsberry (2001) studied the transformation stage of extratropical transition using satellite imagery and model data. They concluded that as the transitioning storm approaches the baroclinic zone, it first experiences increased amounts of VWS before it directly interacts with the baroclinic zone. However, a high-resolution view of the inner core regions was not possible with their data. Our results support their conceptual model. During step 2 of the transformation stage, vertical wind shear induces pronounced asymmetries in the outer region and also in the eyewall.

Strong deep-layer vertical shear exceeding 13 m s^{-1} forced ascent in the downshear direction, and descent in the upshear direction, consistent with balanced dynamics. Contoured frequency by altitude diagrams confirm the predominately upward mass flux in the downshear left quadrant, with predominately downward mass flux in the upshear right quadrant. An elevated reflectivity maximum and updraft in the downshear right quadrant is believed to be indicative of convection initiation. A broad outward-tilted updraft and a strong, contiguous region of radar reflectivity were evident in the downshear left quadrant as precipitation increased. Descent was maximized on the inside edge of the eyewall on the upshear side. The upshear left quadrant was characterized by maturing convection and a combination of deep convective and stratiform precipitation elements. Further maturation and decay of the convection to older, stratiform cells and a prevalence of downdrafts were found in the upshear right quadrant.

Sinlaku's observed structure was similar to previous mesoscale studies of intense storms in the deep tropics impacted by vertical wind shear such as Jimena and Olivia by Black et al. (2002), and Guillermo by Reasor et al. (2009) and Reasor and Eastin (2012). The results are also broadly consistent with the composite structure of sheared storms presented by Reasor et al. (2013). The similarity to the findings in more intense storms suggests that Sinlaku's eyewall structure can largely be explained by the dynamic response to VWS.

Sinlaku's late stage of the tropical cyclone life cycle, weaker intensity, and northerly latitude reveal some differences in the structure of the eyewall convection, however. The analysis suggests that the strongly sheared eyewall itself has characteristics similar to a principal rainband, with a cellular growth region upstream, followed by a contiguous deep convective region, and transition to stratiform precipitation. While the

formation and maturation of individual convective cells does appear to occur, the vertical motion forced by the vertical wind shear appears to form a rainbandlike complex directly in the eyewall. A weaker intensity than that found in previously studied storms may have contributed to the observed structure, enhancing the stratiform component and similarity to rainbands found at outer radii in more intense storms.

While low-level inflow was maximized on the downshear side similar to Reasor et al. (2013), a prominent midlevel inflow was found on the upshear side associated with the increasing prevalence of stratiform precipitation. The upshear midlevel inflow may act to intensify the midlevel circulation through absolute angular momentum convergence above the boundary layer, and may also hinder deep convection by importing low-entropy air into the eyewall. Since the balanced thermal response to a midlevel circulation is cold core, the upshear descent and stratiform precipitation may facilitate extratropical transition to a cold-core system with limited deep convection. Despite the approach to the midlatitudes, no evidence of frontal or cold-core structure was found at this time, indicating that vertical shear dynamics were the dominant mechanism, leading to a tilted, asymmetric tropical storm structure consistent with the three-step transformation proposed by Klein et al. (2000).

Sinlaku's reintensification ended shortly after the observation period, and interaction with the baroclinic zone began to occur on the following day. A detailed SAMURAI analysis, frontogenesis diagnostics, and comparison with ECMWF analysis of Sinlaku on 20 September are presented in a companion paper by Quinting et al. (2014).

Acknowledgments. We thank the international consortium that supported the T-PARC field campaign, the National Center for Atmospheric Research Earth Observing Laboratory for data management and quality control, and ECMWF for access to the operational analyses. Funding for AMF and SCJ was received from the German Research Foundation (DFG) Projects PANDOWAE (FOR896) and from the Helmholtz Foundation ATMO Program. MMB was supported by the National Science Foundation Grant AGS-0851077 and Office of Naval Research Marine Meteorology Grants N001408WR20129 and N000141410118. PAH was supported by the National Science Foundation Grant ATM-0736003 and the Office of Naval Research Marine Meteorology Grant N0001412AF00002. The authors thank Chris Davis for his helpful comments throughout the course of this research, and Michael Riemer and one anonymous reviewer for their careful reviews that helped to improve the initial manuscript.

APPENDIX

SAMURAI Analysis Methodology

The SAMURAI analysis objectively estimates the most likely state of the atmosphere based on various types of observations using a variational technique. It minimizes an incremental form of a cost function using a Galerkin approach, with cubic B-spline finite elements as a basis. In contrast to traditional objective analysis techniques, SAMURAI can specify the error characteristics individually for different instrumentation, it can incorporate more complex observations such as remote sensing data, it can use model fields such as ECMWF fields as background estimates, and it can include balance or physical constraints such as mass continuity. Additional technical details of SAMURAI are provided in Bell et al. (2012).

For the current study, data from ELDORA, dropsondes, aircraft flight level, and satellite atmospheric motion vectors were included in the analysis. C-130 dropsonde data were incorporated into the analysis, but the flight level data were not used because of limitations in quality control of the latter dataset. The analysis was performed in a storm-relative coordinate system, with all observations from 0000 to 0600 UTC time and space corrected to Sinlaku's position at 0400 UTC 19 September using a storm motion of 8.7 m s^{-1} at 66° that was removed from the wind components. An initial coarse-resolution analysis with a horizontal node spacing of 10 km was performed to adjust Sinlaku's general position, intensity, and structure from the operational 25-km ECMWF analysis as an a priori background estimate. The coarse-resolution background state was then used to initialize the high-resolution analysis with a horizontal node spacing of 1 km and vertical node spacing of 0.5 km. The high-resolution domain size was $150 \text{ km} \times 150 \text{ km}$ from the surface to 14 km.

The background state and field experiment observations were combined using the error characteristics listed in Table A1. A Gaussian spatial filter was used to control the spatial influence of the observations, resulting in a spatial resolution of resolved wavelengths above 4 and 2 km in the horizontal and vertical, respectively. Regions with radar reflectivity less than -10.0 dBZ were removed from the final analysis since they were primarily determined by the coarse-resolution background field. The reduced radar range from the aircraft and high sensitivity of the ELDORA receiver allowed for wind retrievals in the cloudy, but nonprecipitating regions in the southeastern open eyewall region.

The unique flight pattern of the NRL P-3 allowed for radar coverage of the complete eyewall, with an overdetermined solution in the southeastern eyewall near

TABLE A1. Samurai configuration details. Standard deviation of the background errors for moist-air-density-weighted wind components (ρu , ρv , and ρw), temperature T , water vapor mixing ratio q_v , and dry-air density ρ_a for the 10- and 1-km analysis.

	$\rho u, \rho v$ ($\text{kg m}^{-2} \text{ s}^{-1}$)	ρw ($\text{kg m}^{-2} \text{ s}^{-1}$)	T (K)	q_v (g kg^{-1})	ρ_a (kg m^{-3})
10 km	10	2	3	3	0.03
1 km	10	10	1	1	0.01

the loop in the flight track (Fig. 2). In theory, the steep elevation angles provided by ELDORA in the southeastern eyewall should produce improved vertical velocity estimates near the loop in the flight track using the full multi-Doppler equations (Armijo 1969). However, numerical instability of the variational solution near the flight track produced an unrealistic vertical velocity pattern in this region when steep elevation angles were included. Wind estimates were greatly improved by limiting the elevation angle to 45° and neglecting the projection of the vertical wind in the Doppler velocity, similar to what is used in a two-radar dual-Doppler solution (Ray et al. 1980). The horizontal divergence is still strongly overdetermined by the nearly orthogonal radar beams such that the vertical velocity determined through mass continuity has a low error (Hildebrand et al. 1996). This novel "hybrid" technique blends the classic dual-Doppler approach with the modern variational assimilation to reduce ill conditioning in the Doppler equations and still avoid explicit integration of the mass continuity equation.

REFERENCES

- Agusti-Panareda, A., C. D. Thorncroft, G. C. Craig, and S. L. Gray, 2004: The extratropical transition of Hurricane Irene (1999): A potential vorticity perspective. *Quart. J. Roy. Meteor. Soc.*, **130**, 1047–1074, doi:10.1256/qj.02.140.
- Aiyyer, A., and C. Thorncroft, 2011: Interannual-to-multidecadal variability of vertical shear and tropical cyclone activity. *J. Climate*, **24**, 2949–2962, doi:10.1175/2010JCLI3698.1.
- Anwender, D., P. A. Harr, and S. C. Jones, 2008: Predictability associated with the downstream impacts of the extratropical transition of tropical cyclones: Case studies. *Mon. Wea. Rev.*, **136**, 3226–3247, doi:10.1175/2008MWR2249.1.
- Armijo, L., 1969: A theory for the determination of wind and precipitation velocities with Doppler radars. *J. Atmos. Sci.*, **26**, 570–573, doi:10.1175/1520-0469(1969)026<0570:ATFTDO>2.0.CO;2.
- Atallah, E. H., and L. F. Bosart, 2003: The extratropical transition and precipitation distribution of Hurricane Floyd (1999). *Mon. Wea. Rev.*, **131**, 1063–1081, doi:10.1175/1520-0493(2003)131<1063:TETAPD>2.0.CO;2.
- Barnes, G. M., E. J. Zipser, D. Jorgensen, and F. Marks Jr., 1983: Mesoscale and convective structure of a hurricane rainband. *J. Atmos. Sci.*, **40**, 2125–2137, doi:10.1175/1520-0469(1983)040<2125:MACSOA>2.0.CO;2.

- Bell, M. M., M. T. Montgomery, and K. E. Emanuel, 2012: Air–sea enthalpy and momentum exchange at major hurricane wind speeds observed during CBLAST. *J. Atmos. Sci.*, **69**, 3197–3222, doi:10.1175/JAS-D-11-0276.1.
- Black, M. L., J. F. Gamache, F. D. Marks, C. E. Samsury, and H. E. Willoughby, 2002: Eastern Pacific Hurricanes Jimena of 1991 and Olivia of 1994: The effect of vertical shear on structure and intensity. *Mon. Wea. Rev.*, **130**, 2291–2312, doi:10.1175/1520-0493(2002)130<2291:EPHJOA>2.0.CO;2.
- Braun, S. A., M. T. Montgomery, and Z. Pu, 2006: High-resolution simulation of Hurricane Bonnie (1998). Part I: The organization of eyewall vertical motion. *J. Atmos. Sci.*, **63**, 19–42, doi:10.1175/JAS3598.1.
- Corbosiero, K. L., and J. Molinari, 2002: The effects of vertical wind shear on the distribution of convection in tropical cyclones. *Mon. Wea. Rev.*, **130**, 2110–2123, doi:10.1175/1520-0493(2002)130<2110:TEOVWS>2.0.CO;2.
- , and —, 2003: The relationship between storm motion, vertical wind shear, and convective asymmetries in tropical cyclones. *J. Atmos. Sci.*, **60**, 366–376, doi:10.1175/1520-0469(2003)060<0366:TRBSMV>2.0.CO;2.
- Davis, C. A., S. C. Jones, and M. Riemer, 2008: Hurricane vortex dynamics during Atlantic extratropical transition. *J. Atmos. Sci.*, **65**, 714–736, doi:10.1175/2007JAS2488.1.
- DeHart, J., R. A. Houze Jr., and R. Rogers, 2014: Quadrant distribution of tropical cyclone inner-core kinematics in relation to environmental shear. *J. Atmos. Sci.*, **71**, 2713–2732, doi:10.1175/JAS-D-13-0298.1.
- DeMaria, M., 1996: The effect of vertical shear on tropical cyclone intensity change. *J. Atmos. Sci.*, **53**, 2076–2088, doi:10.1175/1520-0469(1996)053<2076:TEOVSO>2.0.CO;2.
- , M. Mainelli, L. K. Shay, J. A. Knaff, and J. Kaplan, 2005: Further improvements to the Statistical Hurricane Intensity Prediction Scheme (SHIPS). *Wea. Forecasting*, **20**, 531–543, doi:10.1175/WAF862.1.
- Didlake, A. C., Jr., and R. A. Houze Jr., 2013a: Convective-scale variations in the inner-core rainbands of a tropical cyclone. *J. Atmos. Sci.*, **70**, 504–523, doi:10.1175/JAS-D-12-0134.1.
- , and —, 2013b: Dynamics of the stratiform sector of a tropical cyclone rainband. *J. Atmos. Sci.*, **70**, 1891–1911, doi:10.1175/JAS-D-12-0245.1.
- Frank, W. M., and E. A. Ritchie, 2001: Effects of vertical wind shear on the intensity and structure of numerically simulated hurricanes. *Mon. Wea. Rev.*, **129**, 2249–2269, doi:10.1175/1520-0493(2001)129<2249:EOVWSO>2.0.CO;2.
- Gao, J., M. Xue, K. Brewster, and K. K. Droegemeier, 2004: A three-dimensional variational data analysis method with recursive filter for Doppler radars. *J. Atmos. Oceanic Technol.*, **21**, 457–469, doi:10.1175/1520-0426(2004)021<0457:ATVDAM>2.0.CO;2.
- Harr, P. A., D. Anwender, and S. C. Jones, 2008: Predictability associated with the downstream impacts of the extratropical transition of tropical cyclones: Methodology and a case study of Typhoon Nabi (2005). *Mon. Wea. Rev.*, **136**, 3205–3225, doi:10.1175/2008MWR2248.1.
- Hence, D. A., and R. A. Houze Jr., 2008: Kinematic structure of convective-scale elements in the rainbands of Hurricanes Katrina and Rita (2005). *J. Geophys. Res.*, **113**, D15108, doi:10.1029/2007JD009429.
- , and —, 2011: Vertical structure of hurricane eyewalls as seen by TRMM precipitation radar. *J. Atmos. Sci.*, **68**, 1637–1652, doi:10.1175/2011JAS3578.1.
- Hildebrand, P. H., and Coauthors, 1996: The ELDORA/ASTRAIA airborne Doppler weather radar: High-resolution observations from TOGA COARE. *Bull. Amer. Meteor. Soc.*, **77**, 213–232, doi:10.1175/1520-0477(1996)077<0213:TEADWR>2.0.CO;2.
- Hock, T. F., and J. L. Franklin, 1999: The NCAR GPS dropwindsonde. *Bull. Amer. Meteor. Soc.*, **80**, 407–420, doi:10.1175/1520-0477(1999)080<0407:TNGD>2.0.CO;2.
- Houze, R. A., Jr., 1997: Stratiform precipitation in regions of convection: A meteorological paradox? *Bull. Amer. Meteor. Soc.*, **78**, 2179–2196, doi:10.1175/1520-0477(1997)078<2179:SPIROC>2.0.CO;2.
- , W. C. Lee, and M. M. Bell, 2009: Convective contribution to the genesis of Hurricane Ophelia (2005). *Mon. Wea. Rev.*, **137**, 2778–2800, doi:10.1175/2009MWR2727.1.
- Jones, S. C., 1995: The evolution of vortices in vertical shear. I: Initially barotropic vortices. *Quart. J. Roy. Meteor. Soc.*, **121**, 821–851, doi:10.1002/qj.49712152406.
- , 2000: The evolution of vortices in vertical shear. III: Baroclinic vortices. *Quart. J. Roy. Meteor. Soc.*, **126**, 3161–3186, doi:10.1002/qj.49712657009.
- , 2004: On the ability of dry tropical-cyclone-like vortices to withstand vertical shear. *J. Atmos. Sci.*, **61**, 114–119, doi:10.1175/1520-0469(2004)061<0114:OTAODT>2.0.CO;2.
- Kaplan, J., and M. DeMaria, 2003: Large-scale characteristics of rapidly intensifying tropical cyclones in the North Atlantic basin. *Wea. Forecasting*, **18**, 1093–1108, doi:10.1175/1520-0434(2003)018<1093:LCORIT>2.0.CO;2.
- Klein, P. M., P. A. Harr, and R. L. Elsberry, 2000: Extratropical transition of western North Pacific tropical cyclones: An overview and conceptual model of the transformation stage. *Wea. Forecasting*, **15**, 373–395, doi:10.1175/1520-0434(2000)015<0373:ETOWNP>2.0.CO;2.
- Kuo, H.-C., C.-P. Chang, and C.-H. Liu, 2012: Convection and rapid filamentation in Typhoon Sinlaku during TCS-08/T-PARC. *Mon. Wea. Rev.*, **140**, 2806–2817, doi:10.1175/MWR-D-11-00314.1.
- Lee, W.-C., P. R. Harasti, M. Bell, B. Jou, and M. H. Chang, 2006: Doppler velocity signatures of idealized elliptical vortices. *Terr. Atmos. Oceanic Sci.*, **17**, 429–446.
- Marks, F. D., R. A. Houze Jr., and J. F. Gamache, 1992: Dual-aircraft investigation of the inner core of Hurricane Norbert. Part I: Kinematic structure. *J. Atmos. Sci.*, **49**, 919–942, doi:10.1175/1520-0469(1992)049<0919:DAIOTI>2.0.CO;2.
- Matejka, T., and D. L. Bartels, 1998: The accuracy of vertical velocities from Doppler radar data. *Mon. Wea. Rev.*, **126**, 92–117, doi:10.1175/1520-0493(1998)126<0092:TAOVAV>2.0.CO;2.
- Mohr, C. G., 1988: CEDRIC-Cartesian Space Data Processor. Tech. Rep., National Center for Atmospheric Research, Boulder, CO, 78 pp.
- Montgomery, M. T., and R. J. Kallenbach, 1997: A theory for vortex Rossby-waves and its application to spiral bands and intensity changes in hurricanes. *Quart. J. Roy. Meteor. Soc.*, **123**, 435–465, doi:10.1002/qj.49712353810.
- Moon, Y., and D. S. Nolan, 2010: The dynamic response of the hurricane wind field to spiral rainband heating. *J. Atmos. Sci.*, **67**, 1779–1805, doi:10.1175/2010JAS3171.1.
- Nguyen, L. T., and J. Molinari, 2012: Rapid intensification of a sheared, fast-moving hurricane over the Gulf Stream. *Mon. Wea. Rev.*, **140**, 3361–3378, doi:10.1175/MWR-D-11-00293.1.
- Ooyama, K. V., 1987: Scale controlled objective analysis. *Mon. Wea. Rev.*, **115**, 2479–2506, doi:10.1175/1520-0493(1987)115<2479:SCOA>2.0.CO;2.

- , 2002: The cubic-spline transform method: Basic definitions and tests in a 1D single domain. *Mon. Wea. Rev.*, **130**, 2392–2415, doi:10.1175/1520-0493(2002)130<2392:TCSTMB>2.0.CO;2.
- Quinting, J. F., M. M. Bell, P. A. Harr, and S. C. Jones, 2014: Structural characteristics of T-PARC Typhoon Sinlaku during its extratropical transition. *Mon. Wea. Rev.*, **142**, 1945–1961, doi:10.1175/MWR-D-13-00306.1.
- Ray, P. S., C. L. Ziegler, W. Bumgarner, and R. J. Serafin, 1980: Single- and multiple-Doppler radar observations of tornadic storms. *Mon. Wea. Rev.*, **108**, 1607–1625, doi:10.1175/1520-0493(1980)108<1607:SAMDRO>2.0.CO;2.
- Raymond, D. J., and H. Jiang, 1990: A theory for long-lived mesoscale convective systems. *J. Atmos. Sci.*, **47**, 3067–3077, doi:10.1175/1520-0469(1990)047<3067:ATFLLM>2.0.CO;2.
- Reasor, P. D., and M. D. Eastin, 2012: Rapidly intensifying Hurricane Guillermo (1997). Part II: Resilience in shear. *Mon. Wea. Rev.*, **140**, 425–444, doi:10.1175/MWR-D-11-00080.1.
- , M. T. Montgomery, and L. D. Grasso, 2004: A new look at the problem of tropical cyclones in vertical shear flow: Vortex resiliency. *J. Atmos. Sci.*, **61**, 3–22, doi:10.1175/1520-0469(2004)061<0003:ANLATP>2.0.CO;2.
- , M. D. Eastin, and J. F. Gamache, 2009: Rapidly intensifying Hurricane Guillermo (1997). Part I: Low-wavenumber structure and evolution. *Mon. Wea. Rev.*, **137**, 603–631, doi:10.1175/2008MWR2487.1.
- , R. Rogers, and S. Lorsolo, 2013: Environmental flow impacts on tropical cyclone structure diagnosed from airborne Doppler radar composites. *Mon. Wea. Rev.*, **141**, 2949–2969, doi:10.1175/MWR-D-12-00334.1.
- Riemer, M., and M. T. Montgomery, 2011: Simple kinematic models for the environmental interaction of tropical cyclones in vertical wind shear. *Atmos. Chem. Phys.*, **11**, 9395–9414, doi:10.5194/acp-11-9395-2011.
- , —, and M. E. Nicholls, 2010: A new paradigm for intensity modification of tropical cyclones: Thermodynamic impact of vertical wind shear on the inflow layer. *Atmos. Chem. Phys.*, **10**, 3163–3188, doi:10.5194/acp-10-3163-2010.
- , —, and —, 2013: Further examination of the thermodynamic modification of the inflow layer of tropical cyclones by vertical wind shear. *Atmos. Chem. Phys.*, **13**, 327–346, doi:10.5194/acp-13-327-2013.
- Ritchie, E. A., and R. L. Elsberry, 2001: Simulations of the transformation stage of the extratropical transition of tropical cyclones. *Mon. Wea. Rev.*, **129**, 1462–1480, doi:10.1175/1520-0493(2001)129<1462:SOTTSO>2.0.CO;2.
- Sanabia, E. R., 2010: The re-intensification of Typhoon Sinlaku (2008). Ph.D. thesis, Naval Postgraduate School, Monterey, CA, 213 pp. [Available online at http://edocs.nps.edu/npspubs/scholarly/dissert/2010/Jun/10Jun_Sanabia_PhD.pdf.]
- Schecter, D. A., M. T. Montgomery, and P. D. Reasor, 2002: A theory for the vertical alignment of a quasigeostrophic vortex. *J. Atmos. Sci.*, **59**, 150–168, doi:10.1175/1520-0469(2002)059<0150:ATFTVA>2.0.CO;2.
- Smith, R. K., M. T. Montgomery, and N. V. Sang, 2009: Tropical cyclone spin-up revisited. *Quart. J. Roy. Meteor. Soc.*, **135**, 1321–1335, doi:10.1002/qj.428.
- Tang, B., and K. Emanuel, 2010: Midlevel ventilations constraint on tropical cyclone intensity. *J. Atmos. Sci.*, **67**, 1817–1830, doi:10.1175/2010JAS3318.1.
- Velden, C., and Coauthors, 2005: Recent innovations in deriving tropospheric winds from meteorological satellites. *Bull. Amer. Meteor. Soc.*, **86**, 205–223, doi:10.1175/BAMS-86-2-205.
- Wang, Y., and G. J. Holland, 1996: Tropical cyclone motion and evolution in vertical shear. *J. Atmos. Sci.*, **53**, 3313–3352, doi:10.1175/1520-0469(1996)053<3313:TCMAEI>2.0.CO;2.
- Willoughby, H. E., 1998: Tropical cyclone eye thermodynamics. *Mon. Wea. Rev.*, **126**, 3053–3067, doi:10.1175/1520-0493(1998)126<3053:TCET>2.0.CO;2.
- Yuter, S. E., and R. A. Houze Jr., 1995: Three-dimensional kinematic and microphysical evolution of Florida cumulonimbus. Part II: Frequency distributions of vertical velocity, reflectivity, and differential reflectivity. *Mon. Wea. Rev.*, **123**, 1941–1963, doi:10.1175/1520-0493(1995)123<1941:TDKAME>2.0.CO;2.
- Zipser, E. J., 1977: Mesoscale and convective-scale downdrafts as distinct components of squall-line structure. *Mon. Wea. Rev.*, **105**, 1568–1589, doi:10.1175/1520-0493(1977)105<1568:MACDAD>2.0.CO;2.